Using Multiple MEMS IMUs to form a Distributed Inertial Measurement Unit

THESIS

Ryan Hanson, Second Lieutenant, USAF

AFIT/GE/ENG/05-06

DEPARTMENT OF THE AIR FORCE
AIR UNIVERSITY

AIR FORCE INSTITUTE OF TECHNOLOGY

Wright-Patterson Air Force Base, Ohio

AFIT/GE/ENG/05-06

Using Multiple MEMS IMUs to form a Distributed Inertial Measurement Unit

THESIS

Presented to the Faculty

Department of Electrical and Computer Engineering

Graduate School of Engineering and Management

Air Force Institute of Technology

Air University

Air Education and Training Command

In Partial Fulfillment of the Requirements for the

Degree of Master of Science in Electrical Engineering

Ryan Hanson, B.S.E.E.

Second Lieutenant, USAF

March 2005

AFIT/GE/ENG/05-06

Using Multiple MEMS IMUs to form a Distributed Inertial Measurement Unit

Ryan Hanson, B.S.E.E.

Second Lieutenant, USAF

Approved:

/signed/

_____   _____
Dr. Meir Pachter (Chairman)   date

/signed/

_____   _____
Dr. Peter Maybeck (Member)   date

/signed/

_____   _____
Dr. John Raquet (Member)   date

AFIT/GE/ENG/05-06

Abstract

MEMS IMUs are readily available in quantity and have extraordinary advantages over conventional IMUs in size, weight, cost, and power consumption. However, the poor performance of MEMS IMUs limits their use in more demanding military applications. It is desired to use multiple distributed MEMS IMUs to simulate the performance of a single, more costly IMU, using the theory behind Gyro-Free IMUs. A Gyro-Free IMU (GF-IMU) uses a configuration of accelerometers only to measure the three accelerations and three angular rotations of a rigid body in 3-D space. Theoretically, almost any configuration of six distributed accelerometers yields sufficient measurements to solve for the translational and angular acceleration. In reality, however, sensor noise corrupts the measurements and good sensor geometry is necessary to obtain an accurate estimate of the translational and angular accelerations. Determining the optimal configuration of accelerometers is an exercise in geometry. This thesis investigates the optimal geometry of an INS constructed of multiple networked IMUs and develops the accompanying mechanization and error equations. Simple simulations are run to test and validate the basic design principles.

Acknowledgements

I owe a tremendous debt of gratitude to my thesis advisor Dr. Meir Pachter. His tireless efforts and genuine passion for the theory of guidance and navigation have been an inspiration. Without his help this thesis would not have been possible.

I would also like to thank Dr. Peter Maybeck and Dr. John Raquet for their patience, dedication, and skill as instructors and also for their willingness to serve on my thesis committee.

I want to acknowledge my fellow students Capt. Brian Smith, Maj. Kurt Meidel, and Capt. Mike Starr, as well as Capt. Kevin Biggs and Capt. Kevin Owens. Thanks to you guys I was able to keep my sanity and even have some fun during this very trying experience. Brian, your patience with this butter bar for the last eighteen months has helped me more than you will ever know.

Finally, I must thank my lovely fiancèe. You haven't always understood what I have been working on, but you have never failed to encourage and support me when I needed it. You are the love of my life and I can't wait to be married to you!

To God be all the glory.

Ryan Hanson

Table of Contents

List of Figures

List of Tables

Nomenclature

Reference Frames

i	...	Earth Centered Inertial (ECI) reference frame
e	...	Earth Centered, Earth Fixed (ECEF) reference frame
b	...	Body frame

Standard Notation

$\mathbf{C}$	...	Bold $\mathbf{C}$ designates a Direction Cosine Matrix (DCM)
$\mathbf{X}$	...	Bold letter designates a matrix
X_0	...	Zero subscript designates initial value of X
X_m	...	m subscript designates a measured variable
X_c	...	c subscript designates a calculated variable
δX	...	Error in X, i.e. $X_c = X + \delta X$
$\kappa(\mathbf{X})$	...	Condition number of the $\mathbf{X}$ matrix
$E(X)$	...	Expected value of X
$\mathbf{X}^{\dagger}$	...	Generalized inverse of $\mathbf{X}$

Variables

a	...	Inertial acceleration of the origin of the body frame
a_i	...	Inertial acceleration of point i in the body frame
$\mathbf{C}_x^y$	...	DCM representing a transformation from the x frame to the y frame
$\mathbf{C}_x^y(t)$	...	DCM from the x frame to the y frame at time t
d_i	...	Vector describing the input axis of accelerometer i
$\mathbf{D}$	...	Matrix of accelerometer direction vectors; $\mathbf{D} \triangleq \begin{bmatrix} d_1 \\ \vdots \\ d_N \end{bmatrix}$
$\mathbf{E}$	...	Descriptor matrix, $\mathbf{E} \triangleq \mathbf{H} \cdot \begin{bmatrix} I & 0 \\ 0 & \mathbf{C}_e^b(t) \end{bmatrix}$
$g^{(x)}$	...	Gravitational acceleration, coordinatized in the x frame
$g(r)$	...	Gravitational acceleration, function of position vector r
$\mathbf{H}$	...	Regressor matrix
N	...	Number of accelerometers used in the GF-IMU
$N(\omega)$	...	Nonlinear "disturbance" vector, a vector of $d_i\boldsymbol{\Omega}^2 r_i$ terms
$\mathbf{Q}$	...	Covariance of $\mathbf{E}^{\dagger}$
r	...	position vector
r_i	...	Position vector of accelerometer i in the body frame
$\mathbf{R}$	...	Skew symmetric matrix form of the position vector r
$\mathbf{R}_i$	...	Matrix of accelerometer location vectors; $\mathbf{R}_i \triangleq [r_i...r_N]$
V	...	Measurement noise vector

x_1	...	First 6 navigation states of a GF-IMU, $x_1 = \begin{pmatrix} \omega_{ib}^{(b)} \\ v_{eb}^{(e)} \end{pmatrix}$
x_2	...	Second 6 navigation states of a GF-IMU, $x_2 = \begin{pmatrix} \Psi \\ r^{(e)} \end{pmatrix}$
u	...	Clean measurement
u_m	...	Noise corrupted measurement
y	...	Specific Force
Y	...	Vector of clean specific force measurements, $Y = \begin{pmatrix} y_1 \\ \vdots \\ y_N \end{pmatrix}$
Z	...	Measurement vector
κ	...	Nonlinear kappa filter parameter, $2 \leq \kappa \leq 3$
Ψ	...	Vector of three Euler angles, $\Psi \triangleq [\varphi \ \theta \ \phi]^T$
$\delta\Psi$	...	Error in Euler angles
$\delta\boldsymbol{\Psi}$	...	Error in Euler angles in skew-symmetric form
θ	...	Vector of motion parameters of interest; $\theta \triangleq \begin{pmatrix} \dot{\omega} \\ a \end{pmatrix}$
$\hat{\theta}$	...	Minimum variance estimate of motion parameters
μ	...	Newton's gravitational constant
ω	...	Angular rate of the body frame
$\dot{\omega}$	...	Angular acceleration of the body frame
ω_{xy}	...	Angular rate of the y frame relative to the x frame
$\omega_{xy}^{(z)}$	...	Angular rate of the y frame relative to the x frame and coordinatized in the z frame
$\omega\times$	...	Skew symmetric form of the angular rate vector ω
$\boldsymbol{\Omega}$	...	Skew symmetric form of angular rate vector ω
$\boldsymbol{\Omega}_{xy}^{(z)}$	...	Skew symmetric form of $\omega_{xy}^{(z)}$
Ω_E	...	Earth rate, $= 15^0$ / hour
σ^2	...	Variance of accelerometer measurement noise

Superscripts

$\mathbf{X}^{\dagger}$	...	Generalized inverse of a matrix
T	...	Transpose of a matrix
b	...	Body frame
e	...	Earth Centered, Earth Fixed frame
i	...	Inertial Frame

Subscripts

a	...	Barometric
b	...	Body frame
c	...	Calculated variable
e	...	Earth Centered, Earth Fixed frame
i	...	Inertial Frame
m	...	Measured variable

Using Multiple MEMS IMUs to form a Distributed Inertial Measurement Unit

I. Introduction

In the post-Cold War world, the general trend of developed nations has been to maximize the effectiveness of a small, modern, professional military force while minimizing that force's logistical and maintenance costs. In addition, the emphasis in the methodology of warfighting has increasingly focused on technological and information superiority to achieve the military and political objectives of a conflict at the lowest possible cost, particulary in personnel casualties and collateral damage. This has led to an increased focus on precision guided munitions. Although conventional military formations built around heavy armor are still necessary, recent actions in Somalia (1994), Chechnya (1994-1996 and 1999-present), Afghanistan (2001-present), and most recently Iraq (2003-present), have demonstrated that these formations are poorly suited for the counter-insurgency and guerilla warfare which characterizes the majority of modern conflicts. This new prevalent type of warfare requires mobile, highly trained combined arms forces equipped with accurate weapons systems and the ability to apply them quickly, precisely, and in varying levels of force. The incredible contrast between the area bombing of World War II, only 60 years ago, and the surgical strikes by cruise missiles in the 2003 invasion of Iraq demonstrate the power of this precision. The introduction of Unmanned Aerial Vehicles (UAVs) onto the battlefield has also introduced the need for small, cheap inertial navigation units.

The development of the weapons systems for this new type of warfare is heavily dependent on advances in guidance, navigation, and control, as well as the incorporation and protection of the Global Positioning System (GPS) and its signals. Of increasing importance is the area of low-cost navigation and guidance systems for munitions, UAVs, ballistic missiles, and manned aircraft. As inertial sensor and

computational technology has advanced, the spectrum of available instruments and implementation techniques has widened considerably. These advances have allowed traditional large inertial measurement units mounted on gimbals to be supplanted by smaller, cheaper, and more computationally intensive strapdown units as well as more effective methods of aiding Inertial Navigation Systems (INS) by external means. These developments, together with improvements in GPS and GPS/INS integration, have led to drastically improved navigation and guidance performance at a much smaller cost. This performance is now necessary for many weapons systems currently in use or development that are heavily reliant on accurate navigation information.

The relatively recent marriage of small, cheap, low-grade inertial sensors with GPS has had one of the largest and most visible impacts in the realm of military technology. In the past, the excitement of watching laser-guided bombs striking air vents was offset by their financial expense and the difficult and sometimes dangerous requirement that the target be "painted" with a laser. The advent of weapons guided by a GPS/INS combination, such as the Joint Direct Attack Munition or JDAM, has revolutionized precision warfare by allowing a weapon to be guided by a combination of internal inertial sensors and GPS at a fraction of the cost and without the optical difficulties and increased danger to the operating personnel associated with laser-guided munitions. Overall, the performance and availability of inertial sensors operating within an aided navigation system is now a direct limiting factor in the ability of the Air Force to achieve precision engagement. Advances in inertial sensor technology and aiding directly translate into improved battlefield capabilities for America's armed forces in all types of conflict.

1.1   Problem Definition

The addition of an inertial navigation unit into a weapons system carries a number of costs, including weight, additional power consumption, and volume, as well as the increased financial cost related to acquisition and maintenance. One method of reducing this cost is the replacement of a single, expensive inertial measurement sys-

tem with a system made up of cheaper and more numerous inertial sensors which can match or exceed the same performance. This can be accomplished through the use of multiple distributed Micro-Electric Mechanical Systems (MEMS) IMUs, which are easily many times cheaper than a conventional IMU. MEMS IMUs minimize all of these costs; they are incredibly small, and can be batch produced in large quantities very cheaply. MEMS IMUs are literally flooding the market and are currently triggering a new revolution in inertial navigation, guidance, and control. By optimally combining the measurements of multiple MEMS IMUs, it is possible to achieve improved performance which mimics that of a single, more valuable system. It is therefore necessary to determine the method of optimally combining these measurements and then evaluate potential gains in performance.

1.2   Background to Research

The origin of this research was the **Ant**enna **A**dvanced Inertial **R**eference for **E**nhanced **S**ensors (ANTARES) project, undertaken by AFRL/SNRP [1]. This project was set up to investigate the possibility of emplacing MEMS IMUs at radar aperture locations on aircraft. Inertial measurements from these IMUs can then be used to help compensate for disturbances caused by motion and vibration in RF antennas, specifically GPS and Electronic Support Measures (ESM) antennas, thus improving the overall performance of these systems. It was suggested that these remote sensors could also be used to aid the central INS, and the spinoff of that question led to the motivation for this research.

1.3   Research Objectives

The immediate objective of this research is to establish a solid theoretical foundation for aiding between IMUs using the concept of a Gyro-Free IMU [4]. Utilizing this concept, a distributed configuration of accelerometers is used to determine full information on aircraft motion in all six degrees of freedom. Therefore, emphasis will be on designing a basic system that uses accelerometers to obtain full information on

the translational and rotational acceleration of a rigid body. This system can then be combined with gyroscope and other navigation measurements through the use of a filter to produce the final optimal navigation estimate. This requires determining the optimal geometry used to position the accelerometers and investigating the effects of this geometry on the performance. Ultimately, optimality should include taking into account the ability of the system to withstand sensor failures and continue operation as well as provide the best possible navigation enhancement. However, this research is limited to investigating only the latter, with sensor failure concerns left for future research. The development of the GF-IMU concept, representing the main body of the thesis, will then be followed by Matlab® simulations of GF-IMU mechanization, testing the impact of various accelerometer configurations and quality levels. Finally, a description of a real-life system utilizing the accelerometer and gyroscope measurements of multiple IMUs and relying on the previously developed theory will be discussed in the final chapter.

1.4   Assumptions and Limitations

Due to time limitations, some restrictions were placed on the depth of research. Only terrestrial navigation is considered, although most of the theory is also applicable to extra-terrestrial navigation once changes are made to the gravity model. External aiding of the INS, such as by GPS, is not considered as it is not necessary to the basic theory.

A proper evaluation of the potential performance gains requires in-depth simulations beyond the scope of this paper. Rudimentary simulations are run simply as a proof-of-concept and investigation to validate the theory of geometric optimization. They do not represent a full-scale system performance analysis. A full Kalman filter implementation utilizing a detailed error model would be necessary to gain full information on potential system performance. More complex and realistic simulations are thus left to future work. Also, issues related to identifying and correcting for sensor failure are temporarily ignored in this work but will need to be addressed by future

research. Finally, an important absence is a full mathematical treatment of blending gyro measurements into the GF-IMU concept. This will be discussed but not fleshed out to the extent necessary for implementation. All of these and more are potential subjects for future research built upon the groundwork laid here.

1.5 Thesis Overview

This first chapter has introduced the thesis topic. The second chapter will provide background information on inertial sensors, MEMS technology, INS aiding, and the Gyro-Free IMU concept. The third chapter will build the theory of a GF-IMU and apply this theory to aiding between IMUs, resulting in usable design principles along with mechanization and error equations. The fourth chapter will examine results from simulations. The fifth chapter will summarize the results and their potential impact as well as provide suggestions for future research.

II. Literature Review

2.1 Inertial Navigation

Navigation is the art of planning, recording, and controlling the course and position of a vehicle within a frame of reference. Inertial navigation is a subset of "dead reckoning" navigation [27], in which position is calculated using the sum of a previously determined "initial" position and the measured distance travelled. In inertial navigation, that "distance travelled" is determined using inertial instruments which measure the motion of the vehicle.

According to Newton's first law of motion, an object at rest will remain at rest unless acted upon by an external force. Inertial navigation works by measuring and integrating these external forces over time in order to perform calculations to determine the distance travelled from an initial reference point. Inertial navigation thus gives a relative rather than absolute position, and its performance is limited to the accuracy of the initial position information and the performance of the inertial sensors used.

The greatest advantage of inertial navigation is its ability to operate completely self-contained without any reliance on external radiation or fields. All other forms of navigation are dependent on taking in external electromagnetic radiation, such as light and radio waves, or measurements of the earth's magnetic field, such as by magnetic compass. Navigation relying upon external radiation is susceptible to changes in conditions and to accidental or purposeful interference which may degrade or destroy its effectiveness. Navigation using the earth's magnetic field is imprecise and susceptible to anomalies. From a military perspective, this independence makes inertial navigation ideal for use in military vehicles and weapons. Because inertial navigation requires no external signals, it is impossible to jam or otherwise deny. In addition, it emits no radiation and is impossible to detect. It does not require any human operator, it is not limited to operation within or without the atmosphere, it is completely independent of weather, visibility, and terrain considerations, and, once initialized, it can function automatically without requiring further information.

The drawback of inertial navigation is primarily related to the limitations of inertial sensors themselves. Inertial sensors, as they have so far been developed, yield angular and linear rate and acceleration and measurements rather than direct measurements of position and attitude as desired. It is therefore necessary to integrate the measurements over time in order to determine the change in position and attitude which can be summed to the initial value to determine the new vehicle position. Imperfections in the inertial sensors and, in terrestrial navigation, the complexities of correctly modelling the shape of the earth and its gravitational field produce indistinguishable errors that are also integrated over time so that the accuracy resulting from an independently operating inertial navigation system degrades over time in what is known as "drift". The magnitude of this drift is dependent on the quality of the inertial instruments used.

2.1.1   *The Inertial Measurement Unit (IMU).*   The motion of a body maneuvering in three dimensions can be completely described by six degrees of freedom: linear acceleration along each axis and angular rotation about each axis. Therefore, a mathematical system describing the kinematic motion of the body will have six unknowns and require at least six inputs to achieve a solution. A unit consisting of a set of inertial sensors capable of completely measuring this motion is termed an Inertial Measurement Unit, or IMU. A typical IMU is made up of three linear accelerometers and three rate gyros, with each set arranged in an orthogonal triad. This type of IMU is hereafter referred to as a "conventional IMU".

Accelerometers use precise measurements of the motion of a proof mass to measure specific force, which is the sum of kinematic acceleration and gravitational force-per-unit-mass. Accelerometers are unable to distinguish between these forces which requires that the Inertial Navigation System estimate and remove gravity from the measurements. Typically, an accelerometer senses specific force on one axis, termed the "sensing axis", so that three accelerometers are required in an IMU in order to sense specific force in all three directions. The three accelerometers are normally

aligned on orthogonal axes so that they form a triad. Accelerometer measurements are integrated over time to determine the inertial distance travelled, but yield no information on the direction travelled. As will be demonstrated later in Section 2.2, accelerometers can also be positioned at a distance from the vehicle center of gravity and used to measure the angular acceleration of the body

The rate gyroscopes used in conventional IMUs use a spinning mass or other means such as laser/light radiation to measure angular rate about a single axis. By aligning three gyros on orthogonal axes, an IMU can sense rotation in all directions. Information from the IMU can thus be used to determine the facing, or attitude, of the aircraft by integrating these rotations over time and summing them with an initial estimated attitude. Imperfections and friction within the gyroscope causes measurement errors which drift and tend to increase with time.

2.1.2   The Inertial Navigation System (INS).   The sole function of an IMU is to provide accurate inertial measurements. The INS processes these measurements and uses the initial navigation state of the vehicle and a model of the earth and its gravitational field to project the current navigation state, usually the location, velocity, and attitude of the vehicle. The fundamental concept of an INS can be implemented in various physical mechanizations and coordinate frames. The standard coordinate frames used in this paper will now be described. They will be followed by a description of common mechanizations, with an emphasis on strapdown mechanization which is the most relative to this research's theory.

2.1.3   Coordinate Reference Frames for Terrestrial Navigation.   It is useful to describe a vehicle's position and attitude in multiple reference frames since this allows for different convenient reference frames to be used at certain points in the mechanization.

2.1.3.1   Earth Centered Inertial (ECI) Frame.   All inertial measurements measure motion relative to an inertial frame. The origin of the Earth Centered

Inertial frame is located at the center of the earth with the z axis through the earth's axis of rotation and the x axis passes through the equator and is aligned to a fixed point in space, the First Point of Aries. The y axis is orthogonal to the other two axes. Inertial sensors measure motion with respect to the inertial frame, but it is not very convenient for terrestrial navigation because it does not account for the shape or rotation of the earth. The ECI frame is referenced with a lower case letter "i".

2.1.3.2   Earth Centered Earth Fixed (ECEF) Frame.   The Earth Centered Earth Fixed Frame (ECEF) is very similar to the ECI frame but rotates at the same speed as the earth so that it remains fixed with respect to a point on the earth's surface, making it more useful for terrestrial navigation. The frame is centered on the earth with the z axis through the axis of rotation, the x axis aligned with the Greenwich Meridian, and the y axis orthogonal to complete the set. Translating coordinates from the ECI frame to the ECEF frame is relatively simple, requiring only one rotation about the z axis as a function of time to account for earth rotation. The ECEF frame is referenced with a lower case letter "e".
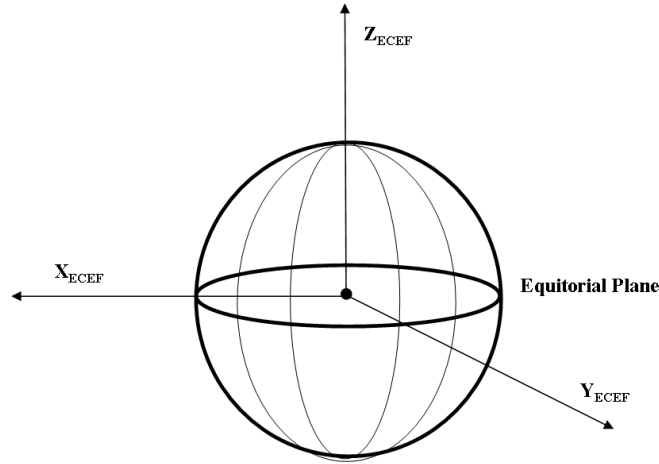
Figure 2.1:   Illustration of the ECEF Frame

2.1.3.3   Navigation Frame.   The Navigation frame measures locations relative to the equator and the Greenwich Meridian using degrees latitude and lon-

gitude with an altitude term defining the distance from the location to the earth's surface. The origin of the Navigation frame is located at the vehicle center of gravity. This frame is the most commonly used for terrestrial navigation but requires more complex transformations from the inertial frame. The Wander Azimuth frame, in more common use, is similar to the Navigation frame but uses a wander azimuth angle rotation to avoid mathematical singularities at high latitudes [21]. The Navigation frame is referenced with a lower case letter "n".

2.1.3.4 Body Frame.   The Body frame is aligned so that its origin is collocated with the center of gravity of the body of interest, such as an airframe, with the z axis aligned vertically, the x axis aligned horizontally with the most likely direction of motion, and the y axis orthogonal to the other two. The body frame is only required if the sensors are attached directly to the body itself, such as in a strapdown mechanization. The body frame moves and rotates with respect to the other earth reference frames dependent on the motion of the body itself. The body frame is referenced with a lower case letter "b".
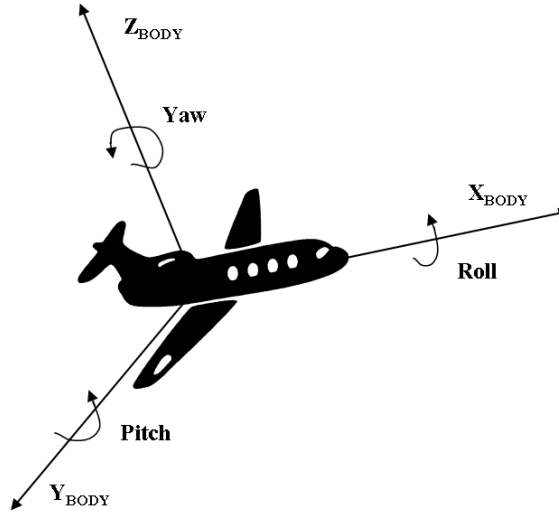
Figure 2.2:   Illustration of the Body Frame

2.1.4 Coordinate Transformations.   There are several methods to accomplish coordinate transformations between reference frames. This paper will use the Direction Cosine Matrix (DCM) method. A DCM can be computed as a product of three rotation matrices, each of which represent a rotation about an individual axis.

The aircraft attitude is given by the vector of ordered Euler angle rotation angles

$$\Psi = \begin{pmatrix} \psi \\ \theta \\ \phi \end{pmatrix} = \begin{pmatrix} \text{Roll angle, relative to x axis} \\ \text{Pitch angle, relative to y axis} \\ \text{Yaw angle, relative to z axis} \end{pmatrix}$$

where the x,y, and z axes are those of the current reference frame. The rotation matrices about each axis are

$$\text{rotation about x axis: } \mathbf{C}_1 = \begin{pmatrix} 1 & 0 & 0 \\ 0 & \cos\phi & \sin\phi \\ 0 & -\sin\phi & \cos\phi \end{pmatrix}$$

$$\text{rotation about y axis: } \mathbf{C}_2 = \begin{pmatrix} \cos\theta & 0 & -\sin\theta \\ 0 & 1 & 0 \\ \sin\theta & 0 & \cos\theta \end{pmatrix}$$

$$\text{rotation about z axis: } \mathbf{C}_3 = \begin{pmatrix} \cos\psi & \sin\psi & 0 \\ -\sin\psi & \cos\psi & 0 \\ 0 & 0 & 1 \end{pmatrix}$$

The total rotation matrix about all three axes is given by the product of all three of these matrices, in 1-2-3 order, i.e. rotating about the z, then y, and then x axis, can then be written:

$$\mathbf{C}_3 \cdot \mathbf{C}_2 \cdot \mathbf{C}_1 = \begin{pmatrix} \cos\theta\cos\psi & -\cos\phi\sin\psi + \sin\phi\sin\theta\cos\psi & \sin\phi\sin\psi + \cos\phi\sin\theta\cos\psi \\ \cos\theta\sin\psi & \cos\phi\cos\psi + \sin\phi\sin\theta\sin\psi & -\sin\phi\cos\psi + \cos\phi\sin\theta\sin\psi \\ -\sin\theta & \sin\phi\cos\theta & \cos\phi\cos\theta \end{pmatrix}$$

The resultant matrix is denoted $\mathbf{C}_x^y$, where x represents the coordinate frame given and y represents the coordinate frame desired. For example, if it is desired to transform a vector r^x coordinatized in the x frame to the y frame, the transformation is accomplished as:

$$r^y = \mathbf{C}_x^y \cdot r^x$$

2.1.5 INS Mechanizations. Inertial Navigation Systems all operate using the same basic principles but there are differing methods of physical implementation. The INS mechanization refers to the physical configuration of the sensors relative to both the vehicle body and the reference frame. The resulting mechanization equations are differential equations describing the navigation states of interest, typically position, velocity, and attitude, as functions of the inertial sensor outputs. The primary types of physical implementation utilize either a stabilized platform or strapdown techniques, both of which are briefly described here.

2.1.5.1 Stabilized Platform Mechanizations. A Space Stabilized (SS) mechanization utilizes a platform stabilized with respect to inertial space [27]. Any angular movement sensed by the inertial instruments for is accounted for and corrected so that the platform remains stationary in the inertial frame. Using this mechanization, all sensor inputs and navigation are resolved in the ECI frame.

A Local Level (LL) stabilized mechanization utilizes a platform stabilized with respect to the surface of the earth. A Local Level mechanization has the advantage that two of the three accelerometer sensing axes are parallel to the ground so that the gravitational force component measured is present in only one accelerometer reading if the platform is perfectly level.

Any type of stabilized platform mechanization incurs a tremendous amount of additional cost. The addition of the gimballed platform and motors to maintain the stabilization add a considerable amount of weight, power consumption, and size. These systems are also more expensive to purchase and maintain and are more likely

to break down due to their preponderance of moving parts. As such, these systems have largely been relegated to expensive strategic applications such as ICBMs and space systems.

    2.1.5.2 Strapdown Mechanization. The vast majority of INS mechanizations in current use are strapdown, in which the inertial sensors are rigidly fixed, or "strapped" to the vehicle body [27]. This has numerous advantages over the stabilized platform mechanizations, not least of which is a drastic decrease in size and weight which allows the incorporation of an INS into very size-sensitive applications such as small aircraft and munitions. The drawbacks of strapdown mechanization are that resolving the measurements requires gyroscopes capable of measuring a much higher rate of turn and a large increase in the overall computational complexity.

Of critical importance in a strapdown mechanization is the DCM describing the transformation from the body frame to the reference frame, typically the Navigation or ECEF frame. This DCM describes the attitude of the vehicle relative to that reference frame and is propagated forward in time using the angular rate measurements.

    2.1.5.3 INS Aiding. Although INS aiding is not a focus of this research, it is worth briefly introducing as part of the larger context of the problem. For a very in-depth study of aiding using Kalman Filtering, please see [12], [13], [14].

Even with an accurate initialization, INS errors cause the navigation solution to drift away from the true values over time, depending on the quality of the sensors. Therefore it is almost always necessary to aid the INS externally with other methods of navigation to help minimize the effects of these errors. Numerous methods of INS-aiding exist, although all are in some way dependent on external sources of radiation. The most well-known is the Global Positioning System (GPS). Navigation by GPS uses radio signals from satellites in space, the positions of which are precisely known, to obtain a direct measurement of position. In addition, there are numerous methods of navigation through the use of radar and radio signals reflecting off of or originating

from the ground (such as Doppler or TACAN). Unfortunately, all methods involving radio or radar waves are subject to atmospheric noise. In addition, hostile forces can detect and/or actively interfere with these signals. Navigation by optical methods uses light emitted by the stars or reflected off the ground to obtain attitude, position, or velocity measurements (such as a star tracker stellar compass [24] or the use of optical flow methodology [30]). Optical methods are dependent on weather and visibility, while the star tracker requires the stars to be visible. Finally, magnetic navigation uses the earth's magnetic field to obtain navigation measurements; while it is obviously difficult to deny, it is nonetheless dependent on an external field and can be degraded by small- or large-scale magnetic anomalies.

GPS has become extremely popular as a navigation aid for INS because it complements the INS error characteristics very well. GPS measurements are corrupted by noise from a variety of sources, but since they translate directly to position, no integration is necessary and the errors do not grow in time. However, the GPS signal can be jammed or even spoofed, so GPS does have a weakness in military applications which anticipate the possibility of operating in an electronic warfare environment. Therefore, the anti-jam capability of a GPS or GPS/INS system is of utmost importance to military applications. Overall, while an INS can yield very precise data that drifts from the truth over time, GPS yields more noisy data that is consistently accurate over time. Many military applications use a combination of GPS and INS, but the effectiveness of these systems is partly dependent on the quality of the INS, especially with respect to attitude which is very difficult to obtain from GPS measurements.

2.2   The GF-IMU Concept

2.2.1   Introduction to the Concept.   As previously stated, the motion of a body maneuvering in three dimensions can be completely described by six degrees of freedom: linear acceleration along each axis and angular rotation about each axis. A conventional Inertial Measurement Unit (IMU) contains six sensors to measure

these six unknowns: three collocated accelerometers and three gyroscopes, arranged in orthogonal triads. However, it is also possible to use six or more distributed accelerometers to form a system capable of measuring the three accelerations and three angular accelerations, and thereby capable of functioning as an IMU; this system is termed a "Gyro-Free IMU" (GF-IMU). An inertial navigation system which navigates using measurements from one or more GF-IMUs is termed a Gyro-Free Inertial Navigation System, or GF-INS.

Because of the greater mechanical complexity of gyroscopes, accelerometers are generally smaller, more cost-effective, and use less power than gyros of a comparable quality classification. Gyro-Free Inertial Navigation Systems also have the advantage of completely avoiding having to account for the notorious gyro error characteristics. This is all the more important when considering using MEMS inertial sensors since, despite many advances, the incorporation of MEMS gyros represents a huge challenge due to their poor performance [3]. Though development is continuing [9], they are not expected to substantially improve in comparison to MEMS accelerometers anytime soon [25]. The theory behind a GF-INS can also be applied to the use of multiple distributed IMUs to obtain improved angular rate measurements.

The major downside of a GF-IMU, as well as any other system that uses accelerometers to measure angular rate, is that only angular acceleration measurements are directly available. Therefore, in a strap-down navigation mechanization an additional integration is required to back out attitude, velocity, and position, leading to errors which grow an order of magnitude faster than in a conventional IMU. This makes the GF-IMU a "fast diverging system" and basically means that the GF-IMU needs to be heavily aided before it can be of much use for navigation.

There is also a performance trade-off relating to the distances between accelerometers, here termed "lever-arms". Larger lever-arms are desired because they increase the ratio of the measurement magnitude over the magnitude of the sensor errors, but arm-lengths which are too large may be impractical or introduce flex modes

which would add a new disturbance. Therefore a balance must be found between the desire to increase the Signal-to-Noise Ratio (SNR) and realistic physical limitations in the design and implementation of the GF-IMU. It is desired to maintain the rigid body assumption, therefore the array size chosen must exhibit disturbances due to flex modes that can be safely ignored given the precision desired out of the GF-IMU system.

The discussion of lever-arms brings up a key distinction that must be made. Larger accelerometer lever-arms increase the magnitude of the measurement for a given angular acceleration, thus decreasing the ratio of the measurement noise in the final signal. In effect, larger lever-arms increase the Signal-to-Noise Ratio of the system. The arrangement, or geometry, of the accelerometer configuration has a similar but separate effect. Good geometry increases the observability of linear and angular accelerations, while bad geometry can make the variables poorly observable or even unobservable. It can be safely assumed that the designer of any system using accelerometers to measure angular acceleration will attempt to optimize performance by utilizing the largest lever-arms feasible without introducing significant disturbances. Therefore, the optimal accelerometer configuration geometry can be normalized and considered as an entirely separate issue, which is the subject of this research. The focus then becomes enhancing the observability of the measurements through the use of geometry.

2.2.2   Previous Work.   The concept of using distributed accelerometers configured to function as a gyroscope-free IMU is at least 30 years old [19], and the concept of using accelerometers to measure rotational acceleration is even older [22]. It has long been known that six accelerometers could yield full information on the 3-D acceleration and rotation of a rigid body. Since a rigid body has six degrees of freedom, and therefore six unknowns, it makes sense that at least six sensor inputs are necessary. Initially, however, it was believed that nine sensors were needed [4]. In 1994, an optimal cube-like configuration of six distributed accelerometers was de-

veloped by DeBra that allows rotational acceleration to be directly calculated as a function of the accelerometer outputs [4].

Some of the most recent and significant research into GF-IMUs has been done for the California PATH program by Chin-Woo Tan and Sungsu Park at the University of California, Berkeley. For the full body of this previous work see [20], [26], and [25]. Their research has developed the criteria for a feasible GF-IMU geometry as well a basic set of equations to relate the accelerometer outputs to the linear and angular accelerations of the moving body. In addition, they have developed a set of error equations encompassing sensor and misalignment errors, conducted basic simulations, and constructed a prototype.

The California PATH program research has been limited to a single configuration, with an emphasis on land navigation aided by GPS. Their approach simply assumes a given geometry and then derives the necessary equations. In contrast, this thesis represents a similar but separate and more methodical approach to GF-IMU theory than previous work by developing a new way to mathematically describe and evaluate GF-IMU configurations. The mechanization and error equations can then be derived more efficiently through the use of this new methodology, with an emphasis on the increased complexity of navigation in three dimensions.

2.3   MEMS Inertial Technology

2.3.1   Brief Introduction.   MEMS is an acronym for "Micro Electronic Mechanical Systems", and is synonymous with the terms Microsystems (Europe) and Micromachines (Japan). The term dates back to a series of workshops on microdynamics and MEMS in 1987 [16] which helped spark the first major development. The field of MEMS inertial devices has become very successful in the automotive industry, with millions of MEMS accelerometers sold each year; other MEMS inertial sensor applications such as the aerospace industry have picked up more more recently, but are entering into a period of rapid growth [16].

In 1993, sales of all types of MEMS were less than \$2 billion; by 2000, MEMS sales had risen to over \$12 billion. [16] Revenues from MEMS gyros sales alone are projected to grow from \$279 million in 2002 to \$396 million in 2007 [2]. Sales are skyrocketing as MEMS inertial sensors are replacing larger conventional sensors or are being used in new applications for which the use of larger conventional sensors is previously impractical. The automotive market, the avionics market, and various military applications continue to drive demand, which in turn encourages continued development at a rapid pace. *Small Times*, a public news source that follows MEMS and nanotechnology development, reports that as of February, 2004, "10 of the top 12 IMU suppliers are either currently offering or actively developing MEMS gyro-based IMUs. And of the more than five-dozen IMUs available, or known to be in development, nearly 50 percent use (or will use) both MEMS gyros and MEMS accelerometers." [2]. Since MEMS devices can be mass produced on wafers, and use a fraction of the power and space of a more conventional inertial sensor, the marketability of MEMS devices is primarily limited by their capabilities which, thanks to tireless research and development, are improving at a fast rate. As another author put it more simply, MEMS are "application driven and technology limited" [16]

2.3.2 Military Incentive. One of the primary factors driving MEMS development in the inertial realm is the prospect of military contracts. As their performance improves, MEMS devices are becoming attractive for an increasing number of military applications, where their small size, low cost, and low power consumption make them ideal in munitions and other small, inexpensive systems. A quick overview of military projects working to incorporate MEMS sensors indicates the large amounts of contract money becoming available for successful MEMS IMU manufacturers:

2.3.2.1 DIG/NU. DIG/NU stands for "Deeply Integrated Guidance and Navigation Unit", and is a program to develop a deeply (ultra-tight) coupled GPS/INS system that fits within five cubic inches utilizing MEMS technology. The resultant device could accurately guide a projectile with the precision of GPS, while

deep integration with a MEMS INS allows for vastly increased anti-jam and loss of lock capability. The GPS and INS systems would be able to share a single processor [10].

2.3.2.2 Army/Marine Corps: Excalibur. The Excalibur (XM982) program aims to develop a 155 mm artillery shell for current and future Army and Marine howitzers utilizing a GPS/INS guidance system with the ability to strike targets 50 km away with a 20m CEP. The Excalibur will function in current US digital howitzers and will also be an integral part of the larger Army concept of a non-line-of-sight cannon (NLOS-C), one of the core elements of the Army Future Force. Development of reliable, gun-hardened MEMS GPS/INS units will yield a direct firepower advantage to US ground forces while reducing logistics demand and collateral damage through improved efficiency of targeting [29].

2.3.2.3 OAV. Another core element of the Army Future Force, designed to help give US troops information superiority, is the Organic Aerial Vehicle, a small UAV designed to operate on the squad and platoon level (two separate versions are planned) and flying using ducted air fans. Because it will have the capacity to "hover and stare", the OAV will give Army commanders a literal eye in the sky to scout out enemy dispositions and gain valuable intelligence on what lies ahead. In this type of vertical/horizontal flight, accurate inertial information about attitude and speed are critical, but the small size of the vehicle limits the weight and power consumption of any inertial units. Thus a perfect application for a high quality MEMS IMU [7].

2.3.2.4 Navy: ERGM. The Navy Extended Range Guided Munition (EX-171) program seeks to develop a 5" GPS/INS guided gun round for accurate naval bombardment and gunfire support of ground forces. The goal is a projectile with a range of 41 nm and a CEP of less than 20 m, utilizing the GPS/INS combination to obtain the maximum anti-jam capability. This technology will be a critical part of the Navy's surface warship development [6].

2.4 Conclusion

This completes the literature review and introduction of topics. The importance and possible benefits of the research have been outlined, and the topics of inertial navigation, Gyro-Free IMUs, and MEMS inertial technology have been introduced. The development of the theory for a Gyro-Free strapdown mechanization in the ECEF reference frame will now follow.

III. Methodology

3.1 Measuring Angular Acceleration using Accelerometers

An accelerometer is a sensor designed to measure specific force, f, along a sensitive (input) axis - also referred to as a Specific Force Receiver (SFR). The specific force is the sum of the kinematic acceleration, a, and the gravitational acceleration, g:

$$f = a - g \tag{3.1}$$

In inertial navigation, one is interested in the kinematic acceleration a, so the acceleration due to gravity, g, must be "subtracted from" the measured specific force f. Thus,

$$a = f + g \tag{3.2}$$

The gravitational acceleration to be removed is calculated from the vehicle's estimated position. Inaccurate accounting for gravity is the source of many error dynamics in an IMU, but can be safely ignored during the initial theoretical development of the GF-IMU, because it can be safely presumed that it is properly accounted for by the INS.

Consider an inertial frame within which exists a body frame; i.e., the body frame can move and rotate within the inertial frame but points in the body frame will remain stationary relative to each other. Let a be the kinematic acceleration of the origin of the body frame, ω be the inertial angular rate of the rigid body, and r_i be the location of a point i in the body frame, for $i = 1, 2, \ldots, N$. The acceleration of point i is a_i. The inertial acceleration of the point i is given by the Coriolis formula:

$$a_i = a + \dot{\omega} \times r_i + \omega \times (\omega \times r_i) \tag{3.3}$$

According to (3.1) the specific force sensed at point i is

$$a_i = a + \dot{\omega} \times r_i + \omega \times (\omega \times r_i) - g \tag{3.4}$$

and the reading y_i of a single-axis accelerometer at location i with input axis orientation d_i in the body frame is given by the fundamental equation:

$$y_i = d_i \cdot a + (\dot{\omega} \times r_i) \cdot d_i + [\omega \times (\omega \times r_i)] \cdot d_i - d_i \cdot g \tag{3.5}$$

We will use the skew symmetric form of ω, $\mathbf{\Omega}$, and the skew symmetric form of r_i, $\mathbf{R_i}$.

$$\mathbf{\Omega} = \begin{bmatrix} 0 & -\omega_3 & \omega_2 \\ \omega_3 & 0 & -\omega_1 \\ -\omega_2 & \omega_1 & 0 \end{bmatrix}$$

$$\mathbf{R_i} = \begin{bmatrix} 0 & -r_{i_z} & r_{i_y} \\ r_{i_z} & 0 & -r_{i_x} \\ -r_{i_y} & r_{i_x} & 0 \end{bmatrix}$$

Applying these to Equation (3.4) yields

$$d_i \cdot (\dot{\omega} \times r_i) = -d_i^T \cdot \mathbf{R_i}\dot{\omega} \tag{3.6}$$

$$[\omega \times (\omega \times r_i)] \cdot d_i = d_i^T \cdot \mathbf{\Omega}^2 r_i \tag{3.7}$$

Inserting Equations (3.6) and (3.7) into Equation (3.4), the fundamental equation can be rewritten as:

$$y_i = a \cdot d_i - d_i^T \mathbf{R_i}\dot{\omega} + d_i^T \mathbf{\Omega}^2 r_i - d_i \cdot g \tag{3.8}$$

Calculating these terms yields the explicit expression:

$$d_i^T \mathbf{R_i}\dot{\omega} = d_i^T \begin{bmatrix} 0 & -r_{z_i} & r_{y_i} \\ r_{z_i} & 0 & -r_{x_i} \\ -r_{y_i} & r_{x_i} & 0 \end{bmatrix} \begin{bmatrix} \dot{\omega}_x \\ \dot{\omega}_y \\ \dot{\omega}_z \end{bmatrix} \tag{3.9}$$

and

$$d_i^T \mathbf{\Omega}^2 r_i = d_i^T \begin{bmatrix} \omega_x \omega_y r_{y_i} + \omega_x \omega_z r_{z_i} - (\omega_y^2 + \omega_z^2) r_{x_i} \\ \omega_x \omega_y r_{x_i} + \omega_y \omega_z r_{z_i} - (\omega_x^2 + \omega_z^2) r_{y_i} \\ \omega_x \omega_z r_{x_i} + \omega_y \omega_z r_{y_i} - (\omega_x^2 + \omega_y^2) r_{y_i} \end{bmatrix} \qquad (3.10)$$

Given this development, it is a simple matter to insert the values for r_i and d_i pertaining to each accelerometer location and orientation for a specific configuration, and thus form a set of linear equations which relate the inertial acceleration a of the origin of the body frame and the angular acceleration $\dot{\omega}$ of the body to the N accelerometer outputs $(y_1, y_2, ..., y_N)$.

3.2   Geometry Optimality Criteria and Calculations

The mathematical criteria for selecting an optimal accelerometer arrangement can now be discussed. The rigid body state is described by its angular and translational accelerations, $\dot{\omega}$ and a. Suppose N accelerometers are used. By stacking up Equation (3.8) N times, a linear system in $\dot{\omega}$ and a is obtained. In matrix notation,

$$y = \mathbf{H}\theta + \begin{pmatrix} d_1^T \mathbf{\Omega}^2 r_1 \\ \vdots \\ d_N^T \mathbf{\Omega}^2 r_N \end{pmatrix} + \begin{bmatrix} d_1^T \\ \vdots \\ d_N^T \end{bmatrix} \cdot g \qquad (3.11)$$

where the vector of unknowns is

$$\theta = \begin{pmatrix} \dot{\omega} \\ a \end{pmatrix}_{6 \times 1}$$

the measurement vector is

$$y = \begin{pmatrix} y_1 \\ \vdots \\ y_N \end{pmatrix}_{N \times 1}$$

and the regressor matrix $\mathbf{H}$ is defined by the individual locations and orientations of the accelerometers making up the GF-IMU as follows:

$$\mathbf{H} = \begin{bmatrix} (r_1 \times d_1)^T & \vdots & d_1^T \\ \vdots & \vdots & \vdots \\ (r_N \times d_N)^T & \vdots & d_N^T \end{bmatrix}_{N \times 6} \tag{3.12}$$

3.2.1 Regressor Matrix Condition Number and Dilution of Precision. Solving a system of linear equations involves inverting the $\mathbf{H}$ matrix. If the matrix is poorly conditioned, measurement errors are magnified in the output. Using the example from [15] to make the point, consider the linear system $\mathbf{H}\theta = z$:

$$\begin{bmatrix} 1 & 1000 \\ 0 & 1 \end{bmatrix} \begin{bmatrix} \theta_1 \\ \theta_2 \end{bmatrix} = \begin{bmatrix} 1000 \\ 1 \end{bmatrix}$$

The solution, easily found, is $\theta_1 = 0$ and $\theta_2 = 1$. Now consider the same system again, this time adding a small error in the measurement vector z.

$$\begin{bmatrix} 1 & 1000 \\ 0 & 1 \end{bmatrix} \begin{bmatrix} \theta_1 \\ \theta_2 \end{bmatrix} = \begin{bmatrix} 1000 \\ 1 + \delta z \end{bmatrix}$$

The solution now yields $\theta_1 = -1000\delta z$ and $\theta_2 = 1 + \delta z$. The error in the input vector relative to the magnitude of the input vector is $\frac{\delta z}{1000}$ while the relative error in the output is $1000\delta z$. Thus, solving the system of equations amplifies the relative error (the inverse of the SNR) by a maximum factor of 10^6, that is, by the condition number κ of the $\mathbf{H}$ matrix [15]. The condition number is defined as

$$\kappa(\mathbf{H}) = \| \mathbf{H} \| \| \mathbf{H}^{-1} \| \tag{3.13}$$

Indeed, assuming that the matrix $\mathbf{H}$ is error free, the magnitude of the error in the output is always bounded according to:

$$\frac{\|\Delta\theta\|}{\|\theta\|} \leq \kappa(\mathbf{H})\frac{\|\Delta z\|}{\|z\|} \tag{3.14}$$

In GPS, the Geometric Dilution of Precision (GDOP) concept relates the effect of geometry on the accuracy of an estimate when noisy pseudo-range measurements are used. The GDOP term, defined as

$$GDOP(\mathbf{H}) \triangleq \sqrt{Tr\left(\mathbf{H}^T\mathbf{H}\right)^{-1}} \tag{3.15}$$

can also be employed here. Two additional DOP values are defined, using the partitions of the $\mathbf{H}$ matrix pertaining to the vector quantities $\dot{\omega}$ and a: The $\mathbf{H}$ matrix can be broken up as

$$\mathbf{H} = \begin{bmatrix} \mathbf{H}_{\dot{\omega}_{3\times N}} & \vdots & \mathbf{H}_{a_{3\times N}} \end{bmatrix}$$

and the two new DOP values can then be defined as

$$\dot{\omega}DOP = \sqrt{Tr\left(\mathbf{H}_{\dot{\omega}}^T\mathbf{H}_{\dot{\omega}}\right)^{-1}} \tag{3.16}$$

$$aDOP = \sqrt{Tr\left(\mathbf{H}_a^T\mathbf{H}_a\right)^{-1}} \tag{3.17}$$

$$\tag{3.18}$$

These new DOP values give some measure of the effectiveness of the GF-IMU geometry in measuring the linear and angular accelerations, in which smaller values indicate better measurements. These DOP values assume full knowledge of the other variable; that is, (3.16) is the DOP value for a assuming full knowledge of $\dot{\omega}$, and (3.17) is the DOP value for $\dot{\omega}$ assuming full knowledge of a.

In summary, the effect of configuration geometry on the accuracy of the acceleration and angular acceleration estimates is captured by the GDOP or, alternatively, as the condition number of the regressor matrix $\mathbf{H}$ [18]. The condition number is

directly proportional to the maximum amplification of the measurement error. The DOP metrics are closely related to the respective acceleration and angular acceleration estimation error covariances. Thus the goal of the configuration optimization is to minimize the condition number of this matrix, $\kappa(\mathbf{H})$, as well as the three DOP metrics. This allows for a "scoring" process which can be used to compare individual configurations against each other. Together, these four criteria can be used as individual metrics to estimate the predicted effectiveness of a given geometric accelerometer arrangements.

3.2.2   Normalizing to the Unit Sphere.   A *crucial* step before invoking the $\kappa(\mathbf{H})$ or GDOP optimality criteria is nondimensionalization. Without this step, the resulting metrics values would be skewed by the size of the array. Instead, it is desired to observe the effect of the geometry alone, while temporarily ignoring lever-arms. Therefore, the acceleration a is scaled according to

$$a \rightarrow \frac{a}{L}$$

where L is a characteristic length, that is, L is the radius of the sphere circumscribing the accelerometer array so that a and $\dot{\omega}$ now have the same units of $\left[\frac{1}{sec^2}\right]$. In the same manner, each r_i is scaled as follows

$$r_i = \frac{r_i}{L}$$

As a result the $\mathbf{R}$ matrix is normalized so that the vectors describing the accelerometer locations are unit vectors. This ensures that all the accelerometer locations fall on or inside the surface of a unit sphere centered at the origin. After the nondimensionalization, the condition number and GDOP of the regressor matrix $\mathbf{H}$ are constant regardless of the accelerometer lever-arms used, that is, the size of the accelerometer cluster, allowing us to predict the effectiveness of the GF-IMU geometry independent of the array size.

3.3 Symmetry and Optimality

It is observed throughout many engineering disciplines and through the study of nature that symmetry and optimality are closely related. The exact origin of this has been the subject of much scientific study, and has philosophical and physiological flavors in addition to mathematical and scientific. For example, studies have shown that the human perception of beauty is closely related to symmetry [5]. Studies in optimality of packaging, aerodynamics, and structural engineering (amid numerous other examples) almost always yield a symmetrical optimal configuration. The solution to the problem of optimally positioning accelerometers in a GF-IMU can thus be rather safely postulated to be a symmetrical configuration.

3.3.1 The Platonic Solids.   If the optimal accelerometer configuration is to be symmetric about all three axes, then the five Platonic solids present themselves as the key to the solution. The Platonic solids are formed by joining together regular polygons (2-D convex figures with equal angles and sides of equal length) to form three dimensional solids. These solids represent the only perfectly symmetrical positioning of points in three dimensional space [28], and thus can be postulated as the ideal method of positioning accelerometers in a GF-IMU. The most basic regular polygon is a triangle; by joining three triangles at each vertex, a tetrahedron is formed, with four faces and resembling a pyramid.

By joining four triangles at each vertex the octahedron is formed, with eight faces and resembling two pyramids joined at their base and pointing in opposite directions.

By joining five triangles at each vertex, the icosahedron is formed, with 20 faces.
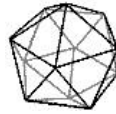
The square is the next regular polygon, and by joining three squares to each vertex the cube is created, with 6 faces.

Finally, the regular pentagon, with an internal angle of 108°, is the last regular polygon which can be used to construct a three dimensional solid. By joining three pentagons to each vertex, the dodecahedron is formed, with 12 faces.
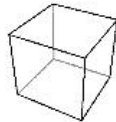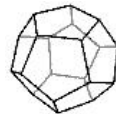

Additional Platonic solids cannot be constructed. Six triangles may be joined at each vertex, but the result forms a plane rather than a solid. More than three squares or pentagons joined at a vertex also fails to form a three dimensional solid. The hexagon, the next regular polygon, cannot be used to create a three dimensional solid. Thus, the set of Platonic solids is limited to the five previously defined (this has been proven many times; for one example, see [17]).

The Platonic solids and some of their geometric properties are listed in Table 3.3.1. A symmetric array of accelerometers aligned using one of these solids could be positioned according to the location of the vertices, the centers of the sides, or the centers of the faces. Thus there are six total configurations that can be directly derived from the Platonic solids, for arrays of 6, 8, 12, 20, and 30 accelerometers. Arrays with an identical number of points, such as the vertices of the tetrahedron and

the faces of the cube (both with six), yield identical configurations. So, a GF-IMU using the minimum number 6 accelerometers could, for example, be based on the geometry of cube faces, tetrahedron edges, or octahedron vertices.

Solid	Vertices	Edges	Faces
Tetrahedron	4	6	4
Cube	8	12	6
Octahedron	6	12	8
Dodecahedron	20	30	12
Icosahedron	12	30	20

Table 3.1:   The Platonic Solids

The Platonic solids can be inscribed into spheres, termed "Platonic Spheres" [17]. Therefore, we refer to a GF-IMU based on the geometry of a Platonic solid as an Inertial Reference Sphere (IRS).

3.3.2 Accelerometer Orientation. Determining the optimal locations (r_i) for the accelerometers is only the first step in defining a GF-IMU geometry. In addition, the orientation of the individual accelerometers (d_i) must be specified. One methodology involves grouping the accelerometers into pairs and aligning the pairs so that the overall configuration can sense angular rotation about each axis, as in the cube configurations in Figures 3.1 and 3.2.

3.3.3 Hamiltonian Circuits. The problem can also be approached using the concept of Hamiltonian circuits from graph theory. A graph consists of a set of vertices connected by edges, while a Hamiltonian circuit is a closed loop path that travels along the edges of a graph and touches each vertex exactly one time. Applying this concept to the problem of aligning accelerometers in a GF-IMU, each accelerometer is located at a vertex and oriented so that its sensitive axis points along an edge towards the next accelerometer in the Hamiltonian path. The idea is to apply a systematic approach to aligning accelerometers that may help shed light on the characteristics of the optimal geometry for a GF-IMU.

In a loose application of this concept, any accelerometer can be pointed toward any other accelerometer, so that N accelerometers yield $(N-1)!$ possible configurations (i.e. for six accelerometers there are 120 configurations to consider). However, by definition, a Hamiltonian path only travels along the defined edges of the Platonic solid, yielding a smaller number of possible configurations (32 for the six-accelerometer case). If isomorphic paths are lumped together, then the number of distinct Hamiltonian paths is further reduced, to 4 for the six-accelerometer case. It is important to note that there is no particular guarantee of optimality through the use of this concept, but it does present a systematic way of examining a large set of possibilities for orientation which may contribute to understanding the geometric characteristics that contribute to optimality. The use of Hamiltonian paths to align accelerometers in a GF-IMU is therefore further explored in Section 3.4.3.

3.4 Six-Accelerometer GF-IMU Configurations

In this research the investigation is first limited to configurations of 6 accelerometers, the minimum amount needed to obtain full information on motion with six degrees of freedom. A configuration using more than 6 accelerometers would be overdetermined, which would improve accuracy and, with additional effort, reliability. Nine-accelerometer configurations will be examined later in this research. It should be kept in mind that all six-accelerometer configurations have been normalized to a unit scale and that the accelerometer locations of each are in fact identical. That is, different shapes represent different rotations of a single perfectly symmetrical array of six points. Thus, the use of different Platonic solids used to identify different six-accelerometer configurations (i.e. the cube, tetrahedron, etc.) are for description and graphical purposes only; in actuality, they all represent the same accelerometer locations rotated in 3-D space. This is *not* true of the accelerometer alignments, which vary with each geometry.

3.4.1 Cube Configurations.   The first two configurations considered are here referred to as cube configurations. These configurations display symmetry in both their accelerometer locations and orientations. Accelerometers are placed on the faces of a cube and aligned in pairs so that each pair measures angular rotation about a different body axis. Thus the total configuration can easily measure rotations in all three axes. In the first cube configuration, accelerometers are located at the center of the faces of the cube and aligned with the edges of the cube shown in Figure 3.1. This configuration is described by the **R** and **D** matrices
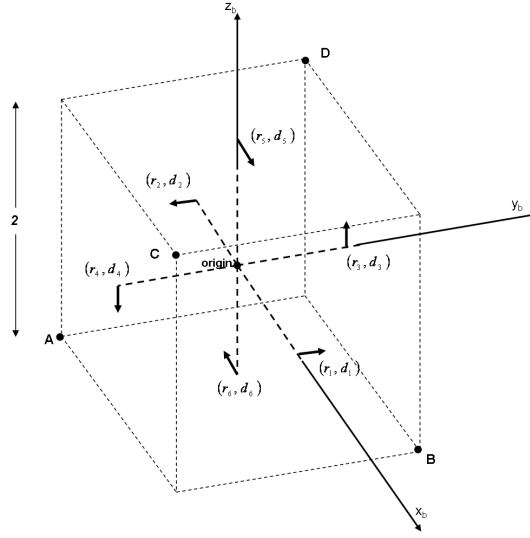

Figure 3.1:   Cube Configuration #1

$$\mathbf{R} = \begin{bmatrix} 1 & -1 & 0 & 0 & 0 & 0 \\ 0 & 0 & 1 & -1 & 0 & 0 \\ 0 & 0 & 0 & 0 & 1 & -1 \end{bmatrix}$$

$$\mathbf{D} = \begin{bmatrix} 0 & 0 & 0 & 0 & 1 & -1 \\ 1 & -1 & 0 & 0 & 0 & 0 \\ 0 & 0 & 1 & -1 & 0 & 0 \end{bmatrix}$$

and is shown in Figure 3.1. The $\mathbf{R}$ matrix is constructed by the N individual r row vectors describing the locations of each accelerometer. The $\mathbf{D}$ matrix is similarly constructed by the N individual row vectors describing the alignment of each accelerometer. The regressor matrix $\mathbf{H}$ which describes the linear system used to solve for the unknowns is thus:

$$\mathbf{H} = \begin{bmatrix} (r_1 \times d_1)^T & \vdots & d_1^T \\ \vdots & \vdots & \vdots \\ (r_N \times d_N)^T & \vdots & d_N^T \end{bmatrix} = \begin{bmatrix} 0 & 0 & 1 & 0 & 1 & 0 \\ 0 & 0 & 1 & 0 & -1 & 0 \\ 1 & 0 & 0 & 0 & 0 & 1 \\ 1 & 0 & 0 & 0 & 0 & -1 \\ 0 & 1 & 0 & 1 & 0 & 0 \\ 0 & 1 & 0 & -1 & 0 & 0 \end{bmatrix}$$

This configuration scores as follows:

$\kappa(\mathbf{H})$	GDOP	$\dot{\omega}$DOP	aDOP
1.000	1.7321	1.2247	1.2247

A second cube configuration, proposed by DeBra in [4], locates the accelerometers on the face of a cube and aligns them toward the vertices, i.e. at a 45 degree slant from the body axes, as shown in Figure 3.2.

$\mathbf{R}$ and $\mathbf{D}$ are now:

$$\mathbf{R} = \begin{bmatrix} 1 & -1 & 0 & 0 & 0 & 0 \\ 0 & 0 & 1 & -1 & 0 & 0 \\ 0 & 0 & 0 & 0 & 1 & -1 \end{bmatrix}$$

$$\mathbf{D} = \frac{1}{\sqrt{2}} \begin{bmatrix} 0 & 0 & -1 & 1 & 1 & 1 \\ 1 & 1 & 0 & 0 & -1 & 1 \\ -1 & 1 & 1 & 1 & 0 & 0 \end{bmatrix}$$

3-12
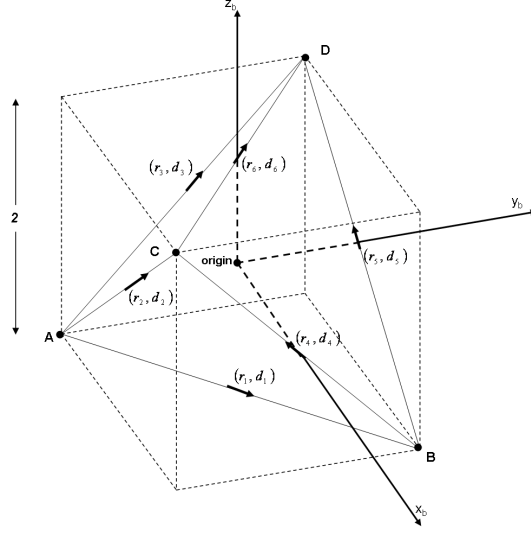
Figure 3.2:   Cube Configuration #2

The regressor matrix $\mathbf{H}$ is thus:

$$\mathbf{H} = \frac{1}{\sqrt{2}} \begin{bmatrix} r_1 \times d_1 & \vdots & d_1^T \\ \vdots & \vdots & \vdots \\ r_N \times d_N & \vdots & d_N^T \end{bmatrix} = \begin{bmatrix} 0 & 1 & 1 & 0 & 1 & -1 \\ 0 & 1 & -1 & 0 & 1 & 1 \\ 1 & 0 & 1 & -1 & 0 & 1 \\ -1 & 0 & 1 & 1 & 0 & 1 \\ 1 & 1 & 0 & 1 & -1 & 0 \\ 1 & -1 & 0 & 1 & 1 & 0 \end{bmatrix}$$

This configuration is scored as follows:

$\kappa(\mathbf{H})$	GDOP	$\dot{\omega}$DOP	aDOP
1.000	1.7321	1.2247	1.2247

Thus, the two cube configurations are equally symmetrical and score identically.

3.4.2 Tetrahedron Configuration.   The third configuration considered is based on the 6 edges of a tetrahedron, but is normalized so that the scale of the configuration is identical to that of the previous cube configurations. An accelerom-
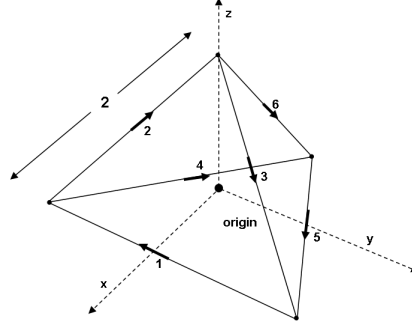
Figure 3.3:   Tetrahedron Configuration

eter is placed at the midpoint of each edge, with the sensitive axes aligned along the edges as shown in the diagram.

$$
\mathbf{R} = \begin{bmatrix} \frac{2}{\sqrt{6}} & \frac{1}{\sqrt{6}} & \frac{1}{\sqrt{6}} & -\frac{1}{\sqrt{6}} & -\frac{1}{\sqrt{6}} & -\frac{2}{\sqrt{6}} \\ 0 & -\frac{1}{\sqrt{2}} & \frac{1}{\sqrt{2}} & -\frac{1}{\sqrt{2}} & \frac{1}{\sqrt{2}} & 0 \\ -\frac{1}{\sqrt{3}} & \frac{1}{\sqrt{3}} & \frac{1}{\sqrt{3}} & -\frac{1}{\sqrt{3}} & -\frac{1}{\sqrt{3}} & \frac{1}{\sqrt{3}} \end{bmatrix}
$$

$$
\mathbf{D} = \begin{bmatrix} 0 & -\frac{1}{2\sqrt{3}} & \frac{1}{2\sqrt{3}} & -\frac{\sqrt{3}}{2} & \frac{\sqrt{3}}{2} & -\frac{1}{\sqrt{3}} \\ -1 & \frac{1}{2} & \frac{1}{2} & \frac{1}{2} & \frac{1}{2} & 0 \\ 0 & \frac{2}{\sqrt{6}} & -\frac{2}{\sqrt{6}} & 0 & 0 & -\frac{2}{\sqrt{6}} \end{bmatrix}
$$

The accelerometer positions in R are normalized to the same magnitude as the cube configurations above. This configuration scores as follows:

$\kappa(\mathbf{H})$	GDOP	$\dot{\omega}$DOP	aDOP
1.4142	3.0000	2.4495	1.7321

3-14
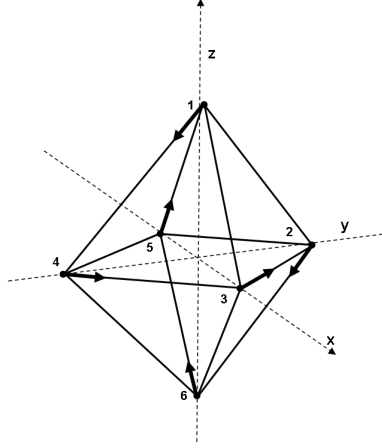
Figure 3.4:   Sample Hamiltonian Path: $1 \rightarrow 4 \rightarrow 3 \rightarrow 2 \rightarrow 6 \rightarrow 5$

3.4.3   Hamiltonian Path Configurations.   Another possible six-accelerometer configuration places accelerometers at the vertices of an octahedron. The normalized locations are:

$$r_{1,2,3,4,5,6} = \begin{pmatrix} 0 \\ 0 \\ 1 \end{pmatrix}, \begin{pmatrix} 0 \\ 1 \\ 0 \end{pmatrix}, \begin{pmatrix} 1 \\ 0 \\ 0 \end{pmatrix}, \begin{pmatrix} 0 \\ -1 \\ 0 \end{pmatrix}, \begin{pmatrix} -1 \\ 0 \\ 0 \end{pmatrix}, \begin{pmatrix} 0 \\ 0 \\ -1 \end{pmatrix}$$

The sensing directions can then be determined through the use of the concept of Hamiltonian paths in graph theory. A path can be defined using a six - element vector, with each accelerometer pointing towards the next one in the list, and the last pointing back to the first to complete the circuit (see Figure 3.4). Using this method, there are 5! (or 120) total configurations possible, 32 of which are true Hamiltonian paths which only travel along the defined edges of the octahedron, (i.e., accelerometer 6 cannot point toward accelerometer 1). By grouping isomorphic paths, there are only four fundamental paths. Without loss of generality, all paths can be assumed to originate at accelerometer 1. One set of paths are those which touch accelerometer 6 as the third point, and a second set are those which touch it at the 5th point. The remaining two sets touch accelerometer 6 on the 4th point and are

3-15

differentiated by whether the 3rd and 5th points are adjacent or diagonal. The results
of scoring these four fundamental paths is as follows:

Fundamental set of paths	$\kappa(\mathbf{H})$	GDOP	$\dot{\omega}$	aDOP
Touches Accel. 6 as 3rd point	∞	∞	1.7321	1.354
Touches Accel. 6 as 4th point, points 3 and 5 adjacent	2.000	2.2913	1.7321	1.5
Touches Accel. 6 as 4th point, points 3 and 5 diagonal	∞	∞	1.7321	1.354
Touches Accel. 6 as 5th point	∞	∞	1.7321	1.354

Table 3.2:   Hamiltonian Path Configurations Calculation Results

The results show that only one family of paths produces a useful $\mathbf{H}$ matrix.
Since all paths are based on an identical $\mathbf{R}$ matrix, the difference lies in the $\mathbf{D}$ matrix
that the path produces. The $\mathbf{D}$ matrices that produce working regressor matrices
all share a common property in that each accelerometer is mirrored by an opposite
accelerometer that senses acceleration in the same plane at an opposite angle, similar
to the DeBra cube in Figure 3.2. The difference is that the DeBra cube ensures that
the sensing direction of each accelerometer is fully orthogonal to the accelerometer's
location vector. In configurations built on a Hamiltonian path, this is not possible,
since the sensing direction vector is always 45° off of the accelerometer position vector.
Therefore a configuration built on a Hamiltonian path with the limitations listed here
cannot score higher than an $\mathbf{H}$ matrix condition number of 2.000. Thus Hamiltonian
paths are not an optimal way to align a GF-IMU, but can help illustrate some desirable
properties.

3.5   Nine-Accelerometer GF-IMU Configurations

The same theory can be extended to the case of 9 distributed accelerometers.
The resulting $\mathbf{H}$ matrix will be 9×6 with a rank of 6. This is a prelude to the analysis
of 3 IMUs, each containing a triad of three collocated accelerometers.

3.5.1   Ideal Cube Extension.   This configuration is formed by adding a triad
of accelerometers at the origin of a the standard 6 accelerometer cube configuration,

with its three orthogonal sensing directions pointing down each of the axes of the body frame. It has the advantage of being highly symmetrical. The result is shown in Figure 3.5. The configuration is defined by:
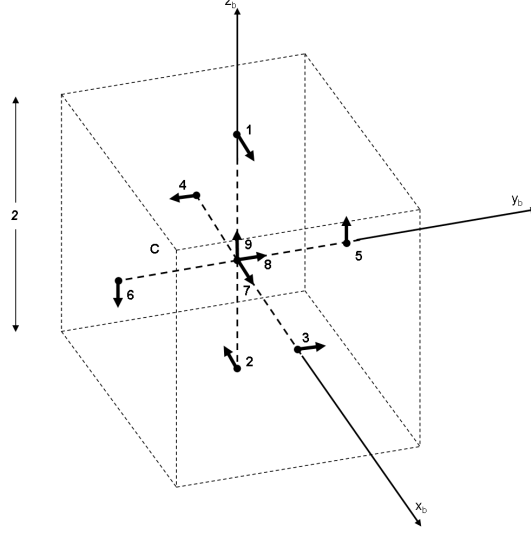

Figure 3.5:   9 Accelerometer Configuration with Triad at Center

$$
\mathbf{R} = \begin{bmatrix} 1 & -1 & 0 & 0 & 0 & 0 & 0 & 0 & 0 \\ 0 & 0 & 1 & -1 & 0 & 0 & 0 & 0 & 0 \\ 0 & 0 & 0 & 0 & 1 & -1 & 0 & 0 & 0 \end{bmatrix}
$$

$$
\mathbf{D} = \begin{bmatrix} 0 & 0 & 0 & 0 & 1 & -1 & 1 & 0 & 0 \\ 1 & -1 & 0 & 0 & 0 & 0 & 0 & 1 & 0 \\ 0 & 0 & 1 & -1 & 1 & 0 & 0 & 0 & 1 \end{bmatrix}
$$

3-17

The resultant $\mathbf{H}$ matrix is:

$$\mathbf{H} = \begin{bmatrix} 0 & 0 & 1 & 0 & 1 & 0 \\ 0 & 0 & 1 & 0 & -1 & 0 \\ 1 & 0 & 0 & 0 & 0 & 1 \\ 1 & 0 & 0 & 0 & 0 & -1 \\ 0 & 1 & 0 & 1 & 0 & 0 \\ 0 & 1 & 0 & -1 & 0 & 0 \\ 0 & 0 & 0 & 1 & 0 & 0 \\ 0 & 0 & 0 & 0 & 1 & 0 \\ 0 & 0 & 0 & 0 & 0 & 1 \end{bmatrix}$$

The configuration scores as follows:

$\kappa(\mathbf{H})$	GDOP	$\dot{\omega}$DOP	aDOP
1.2247	1.5811	1.2247	1.000

It can be seen that the regressor matrix pertaining to this configuration has a larger condition number and smaller GDOP than the original 6-accelerometer cube configuration. The higher condition number is due to the location of the triad at the origin, which yields no arm length and reduces the measurement efficiency, while the lower GDOP and aDOP are due to the improved translational acceleration measurement through the addition of an accelerometer on each axis. Note that the $\dot{\omega}$ term is unchanged; the triad at the origin has no arm length and therefore contributes no angular acceleration measurement. Adding a triad to the center of the second cube configuration has an identical effect.

3.5.2   Nine Distributed Accelerometers.   A configuration utilizing 9 distributed accelerometers as shown in Figure 3.6 is positioned using the vertices and center of a cube so that acceleration in each body frame axis is measured by 3 ac-
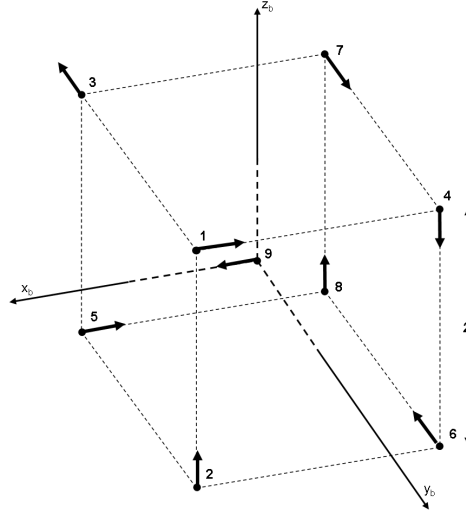
Figure 3.6:   9 Accelerometer Configuration

celerometers. The **R** matrix of the configuration is:

$$\mathbf{R} = \frac{1}{\sqrt{3}} \begin{bmatrix} 1 & 1 & 1 & -1 & 1 & -1 & -1 & -1 & 0 \\ 1 & 1 & -1 & 1 & -1 & 1 & -1 & -1 & 0 \\ 1 & -1 & 1 & 1 & -1 & -1 & 1 & -1 & 0 \end{bmatrix}$$

And the **D** matrix will is:

$$\mathbf{D} = \begin{bmatrix} -1 & 0 & 0 & 0 & -1 & 0 & 0 & 0 & 1 \\ 0 & 0 & -1 & 0 & 0 & -1 & 1 & 0 & 0 \\ 0 & 1 & 0 & -1 & 0 & 0 & 0 & 1 & 0 \end{bmatrix}$$

The regressor **H** matrix is then:

$$
\mathbf{H} =
\begin{bmatrix}
0 & -\frac{1}{\sqrt{3}} & \frac{1}{\sqrt{3}} & -1 & 0 & 0 \\[2ex]
\frac{1}{\sqrt{3}} & -\frac{1}{\sqrt{3}} & 0 & 0 & 0 & 1 \\[2ex]
\frac{1}{\sqrt{3}} & 0 & -\frac{1}{\sqrt{3}} & 0 & -1 & 0 \\[2ex]
-\frac{1}{\sqrt{3}} & -\frac{1}{\sqrt{3}} & 0 & 0 & 0 & -1 \\[2ex]
0 & -\frac{1}{\sqrt{3}} & -\frac{1}{\sqrt{3}} & -1 & 0 & 0 \\[2ex]
-\frac{1}{\sqrt{3}} & 0 & \frac{1}{\sqrt{3}} & 0 & -1 & 0 \\[2ex]
-\frac{1}{\sqrt{3}} & 0 & -\frac{1}{\sqrt{3}} & 0 & 1 & 0 \\[2ex]
-\frac{1}{\sqrt{3}} & \frac{1}{\sqrt{3}} & 0 & 0 & 0 & 1 \\[2ex]
0 & 0 & 0 & 1 & 0 & 0
\end{bmatrix}
$$

The configuration scores as follows:

$\kappa(\mathbf{H})$	GDOP	$\dot{\omega}$DOP	aDOP
2.618	1.9706	1.4745	1.000

3.5.3 Three-IMU Configuration. We now consider a nine-accelerometer array made up of three accelerometer triads, as would typically be found in 3 distributed IMUs. The optimal positioning of these triads can be reduced to positioning on a plane since three points are always collocated on a plane. The triads can be positioned as on the circumference of a circle with radius 1, equally spaced from each other and from the origin. The triads are aligned with the body axes, so that the z axis is perpendicular to the plane. This yields a configuration as shown in Figure 3.7, which displays symmetry. Using the previously defined method of scoring configurations,
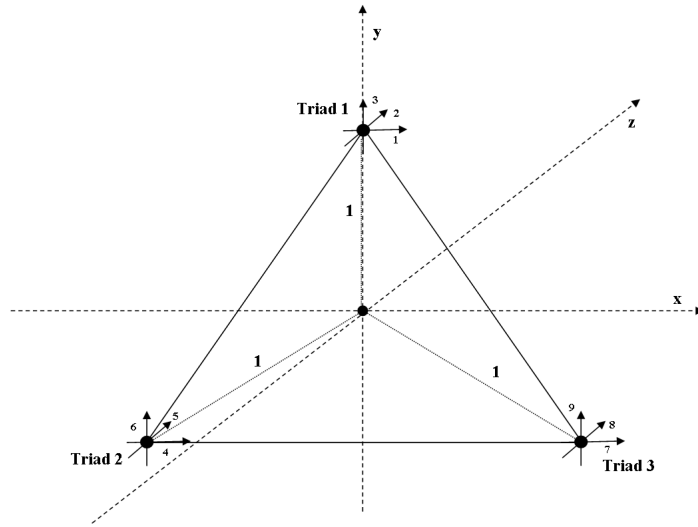
Figure 3.7:   3 Accelerometer Triads

the $\mathbf{R}, \mathbf{D}$, and $\mathbf{H}$ matrices pertaining to this symmetric arrangement are:

$$\mathbf{R} = \begin{bmatrix} 0 & 0 & 0 & -\frac{\sqrt{3}}{2} & -\frac{\sqrt{3}}{2} & -\frac{\sqrt{3}}{2} & \frac{\sqrt{3}}{2} & \frac{\sqrt{3}}{2} & \frac{\sqrt{3}}{2} \\[2mm] 1 & 1 & 1 & -\frac{1}{2} & -\frac{1}{2} & -\frac{1}{2} & -\frac{1}{2} & -\frac{1}{2} & -\frac{1}{2} \\[2mm] 0 & 0 & 0 & 0 & 0 & 0 & 0 & 0 & 0 \end{bmatrix}$$

$$\mathbf{D} = \begin{bmatrix} 1 & 0 & 0 & 1 & 0 & 0 & 1 & 0 & 0 \\ 0 & 1 & 0 & 0 & 1 & 0 & 0 & 1 & 0 \\ 0 & 0 & 1 & 0 & 0 & 1 & 0 & 0 & 1 \end{bmatrix}$$

As a result, the regressor matrix $\mathbf{H}$ is calculated as

$$
\mathbf{H} =
\begin{bmatrix}
0 & 0 & -1 & 1 & 0 & 0 \\
0 & 0 & 0 & 0 & 1 & 0 \\
1 & 0 & 0 & 0 & 0 & 1 \\
0 & 0 & \frac{1}{2} & 1 & 0 & 0 \\
0 & 0 & -\frac{\sqrt{3}}{2} & 0 & 1 & 0 \\
-\frac{1}{2} & \frac{\sqrt{3}}{2} & 0 & 0 & 0 & 1 \\
0 & 0 & \frac{1}{2} & 1 & 0 & 0 \\
0 & 0 & \frac{\sqrt{3}}{2} & 0 & 1 & 0 \\
-\frac{1}{2} & -\frac{\sqrt{3}}{2} & 0 & 0 & 0 & 1
\end{bmatrix}
$$

Running the standard calculations with this $\mathbf{H}$ matrix produces the following score:

$\kappa(\mathbf{H}$	GDOP	$\dot{\omega}$DOP	aDOP
1.4142	1.6330	1.2910	1.000

3.5.4   Summary of Configurations.

# Accel.	Configuration	Condition Number	GDOP	$\dot{\omega}$DOP	aDOP
6	Straight Cube	1.000	1.7321	1.2247	1.2247
6	Slant Cube	1.000	1.7321	1.2247	1.2247
6	Tetrahedron	1.4142	3.0000	2.4495	1.7321
9	Modified Straight Cube	1.2247	1.5811	1.2247	1.000
9	Distributed	2.618	1.9706	1.4745	1.000
9	Three Triads	1.4142	1.6330	1.2910	1.000

Table 3.3:   Results of Configuration Calculations

This table summarizes the results of the calculations for varying GF-IMU configurations. The condition number term shows the theoretical geometric degree of optimality of different potential GF-IMU configurations. It does not by any means indicate the overall supremacy of any configuration, since it does not take into account other restrictions such as the physical space available to implement the GF-IMU array or the accelerometer types or amounts available. The DOP indicates the estimated performance due to geometry but is subject to certain limitations, as described in Section 3.2.1.

3.6 GF-IMU Mechanization Equations

Because of the uniqueness of the GF-IMU concept, it is necessary to start from scratch in the development of the mechanization. Conventional IMU mechanizations do not apply, and previously derived GF-IMU mechanizations are limited to a specific geometry. In a standard conventional INS there are 9 navigation states: three position states, three velocity states, and three attitude states. In a GF-IMU, angular acceleration is measured instead of angular rate; therefore, three angular rate states are added for a total of 12 navigation states. The mechanization equations for a GF-IMU in the ECEF frame are now developed.

Define the constant matrices $\mathbf{A}_{\dot{\omega}}$ and $\mathbf{A}_a$,

$$\begin{bmatrix} \mathbf{A}_{\dot{\omega}_{3 \times N}} \\ \ldots \\ \mathbf{A}_{a_{3 \times N}} \end{bmatrix} \triangleq (\mathbf{H}^T \mathbf{H})^{-1} \mathbf{H}^T$$

and the ω-dependent vectors representing the effect of the non-linearity term $N(\omega)$ defined in Section 3.1,

$$
\begin{bmatrix} f_{\dot{\omega}}(\omega_{ib}^{(b)}) \\ \dots \\ f_a(\omega_{ib}^{(b)}) \end{bmatrix} \triangleq (\mathbf{H}^T\mathbf{H})^{-1}\mathbf{H}^T N(\omega_{ib}^{(b)})
$$

$$
= \begin{bmatrix} \mathbf{A}_{\dot{\omega}} \\ \dots \\ \mathbf{A}_a \end{bmatrix} \cdot N(\omega_{ib}^{(b)})
$$

Note that when $\mathbf{H}$ is non-singular and six accelerometers are used $(N = 6)$,

$$(\mathbf{H}^T\mathbf{H})^{-1}\mathbf{H} = \mathbf{H}^{-1} \tag{3.19}$$

Using the definitions from above, after inversion we obtain the two equations

$$\dot{\omega}_{ib}^{(b)} = -f_{\dot{\omega}}(\omega_{ib}^{(b)}) + \mathbf{A}_{\dot{\omega}} \cdot \mathbf{D} \cdot g^{(b)}(r) + \mathbf{A}_{\dot{\omega}} \cdot Z \tag{3.20}$$

$$a^{(b)} = -f_a(\omega_{ib}^{(b)}) + \mathbf{A}_a \cdot \mathbf{D} \cdot g^{(b)}(r) + \mathbf{A}_a \cdot Z \tag{3.21}$$

where $g^{(b)}(r)$ is the gravitational acceleration calculated as a function of r, the position of the aircraft in the ECEF frame. Equation (3.20) is a differential equation which is integrated to yield $\omega_{ib}^{(b)}$. The $\omega_{ib}^{(b)}$ term is then used in Equation (3.21), which gives the rectilinear acceleration vector.

We now desire to derive the differential equation which can be used to propagate forward the Body to ECEF DCM, $\mathbf{C}_b^e$. We know that

$$\omega_{ib} = \omega_{ie} + \omega_{eb} \tag{3.22}$$

and therefore

$$\omega_{ib}^{(b)} = \mathbf{C}_e^b \omega_{ie}^{(e)} + \omega_{eb}^{(b)} \tag{3.23}$$

We will now apply the first of several mathematical arguments, also known as a Lemmas:

<u>Lemma 1</u>

The skew-symmetric form of a vector which undergoes a coordinate transformation from the ECEF frame to the body frame,

$$v^{(b)} = \mathbf{C}_e^b v^{(e)}$$

is

$$\mathbf{V}^{(b)} = \mathbf{C}_e^b \mathbf{V}^{(e)} \mathbf{C}_b^e$$

$\square$

Using a similarity transformation to obtain the skew symmetric form of $\omega_{ie}^{(b)} = \mathbf{C}_e^b \omega_{ie}^{(e)}$, we have

$$\mathbf{\Omega}_{eb}^{(b)} = \mathbf{\Omega}_{ib}^{(b)} - \mathbf{C}_e^b \mathbf{\Omega}_{ie}^{(e)} \mathbf{C}_b^e \qquad (3.24)$$

Therefore, since

$$\dot{\mathbf{C}}_b^e = \mathbf{C}_b^e \mathbf{\Omega}_{eb}^{(b)}$$

we can write

$$\dot{\mathbf{C}}_b^e = \mathbf{C}_b^e \left(\mathbf{\Omega}_{ib}^{(b)} - \mathbf{C}_e^b \mathbf{\Omega}_{ie}^{(e)} \mathbf{C}_b^e \right)$$
$$= \mathbf{C}_b^e \mathbf{\Omega}_{ib}^{(b)} - \mathbf{\Omega}_{ie}^{(e)} \mathbf{C}_b^e \qquad (3.25)$$

The Earth angular rate in the ECEF frame is

$$\omega_{ie}^{(e)} = \Omega_E \begin{pmatrix} 0 \\ 0 \\ 1 \end{pmatrix}$$

3-25

where Ω_E is approximately 15° an hour. Therefore,

$$\mathbf{\Omega}_{ie}^{(e)} = \Omega_E \begin{bmatrix} 0 & -1 & 0 \\ 1 & 0 & 0 \\ 0 & 0 & 0 \end{bmatrix}$$

and

$$\dot{\mathbf{C}}_b^e = \mathbf{C}_b^e \mathbf{\Omega}_{ib}^{(b)} + \Omega_E \begin{bmatrix} 0 & 1 & 0 \\ -1 & 0 & 0 \\ 0 & 0 & 0 \end{bmatrix} \mathbf{C}_b^e \qquad (3.26)$$

The mechanization equations for navigating in the ECEF frame can now be written. The subscript c designates a calculated variable. Equation (3.20) gives

$$\dot{\omega}_{ib_c}^{(b)} = -f_{\dot\omega}(\omega_{ib_c}^{(b)}) + \mathbf{A}_{\dot\omega} \cdot \mathbf{D} \cdot \mathbf{C}_{e_c}^b \cdot g^{(e)}(r_c^{(e)}) + \mathbf{A}_{\dot\omega} \cdot Z$$

and Equation (3.26) gives

$$\dot{\mathbf{C}}_{b_c}^e = \mathbf{C}_{b_c}^e \mathbf{\Omega}_{ib_c}^{(b)} + \Omega_E \begin{bmatrix} 0 & 1 & 0 \\ -1 & 0 & 0 \\ 0 & 0 & 0 \end{bmatrix} \cdot \mathbf{C}_{b_c}^e$$

The Coriolis formula and Equation (3.21) yields

$$\dot{v}_{eb_c}^{(e)} = \mathbf{C}_{b_c}^e \cdot [-f_a(\omega_{ib_c}^{(b)}) + \mathbf{A}_a \cdot \mathbf{D} \cdot \mathbf{C}_{e_c}^b \cdot g^{(e)}(r_c^{(e)}) + \mathbf{A}_a \cdot Z]$$
$$- 2\Omega_E \begin{bmatrix} 0 & -1 & 0 \\ 1 & 0 & 0 \\ 0 & 0 & 0 \end{bmatrix} \cdot v_{eb_c}^{(e)} - \omega_{ie}^{(e)} \times [\omega_{ie}^{(e)} \times r_c^{(e)}]$$

Finally

$$\dot{r}_c^{(e)} = v_{eb_c}^{(e)}$$

Assuming that the aircraft is initially at rest, the initial conditions are given by

$$\mathbf{C}^e_{b_c}(0) = \mathbf{C}^e_{b_0}$$

$$\omega^{(b)}_{ib_c}(0) = \mathbf{C}^b_{e_0} \cdot \omega^{(e)}_{ie}$$

$$v^{(b)}_{eb}(0) = 0$$

$$r^{(e)}(0) = r^{(e)}_0$$

We note that

$$-\omega^{(e)}_{ie} \times [\omega^{(e)}_{ie} \times r^{(e)}_c] = \Omega^2_E \begin{bmatrix} 1 & 0 & 0 \\ 0 & 1 & 0 \\ 0 & 0 & 0 \end{bmatrix} \cdot r^{(e)}_c$$

and

$$\omega^{(b)}_{ib_c}(0) = \Omega_E (\mathbf{C}^e_{b_0})^T \cdot \begin{pmatrix} 0 \\ 0 \\ 1 \end{pmatrix}$$

The mechanization equations in the ECEF reference frame for a GF-IMU can now be written in their final form. These equations replace the standard IMU mechanization equations used in conventional INS and represents a new contribution to the GF-IMU concept.

$$\dot{\omega}_{ib_c}^{(b)} = -f_{\dot{\omega}}(\omega_{ib_c}^{(b)}) + \mathbf{A}_{\dot{\omega}} \cdot \mathbf{D} \cdot \mathbf{C}_{e_c}^{b} \cdot g^{(e)}(r_c^{(e)}) + \mathbf{A}_{\dot{\omega}} \cdot Z, \quad \omega_{ib_c}^{(b)}(0) = \Omega_E (\mathbf{C}_{b_0}^{e})^T \begin{pmatrix} 0 \\ 0 \\ 1 \end{pmatrix}$$

$$(3.27)$$

$$\dot{\mathbf{C}}_{b_c}^{e} = \mathbf{C}_{b_c}^{e} \Omega_{ib_c}^{(b)} + \Omega_E \begin{bmatrix} 0 & 1 & 0 \\ -1 & 0 & 0 \\ 0 & 0 & 0 \end{bmatrix} \cdot \mathbf{C}_{b_c}^{e}, \quad \mathbf{C}_{b_c}^{e}(0) = \mathbf{C}_{b_0}^{e} \tag{3.28}$$

$$\dot{v}_{eb_c}^{(e)} = \mathbf{C}_{b_c}^{e} \cdot [-f_a(\omega_{ib_c}^{(b)}) + \mathbf{A}_a \cdot \mathbf{D} \cdot \mathbf{C}_{e_c}^{b} \cdot g^{(e)}(r_c^{(e)}) + \mathbf{A}_a \cdot Z]$$

$$+ 2\Omega_E \begin{bmatrix} 0 & 1 & 0 \\ -1 & 0 & 0 \\ 0 & 0 & 0 \end{bmatrix} \cdot v_{eb_c}^{(e)} + \Omega_E^2 \begin{bmatrix} 1 & 0 & 0 \\ 0 & 1 & 0 \\ 0 & 0 & 0 \end{bmatrix} \cdot r_c^{(e)}, \quad v_{eb}^{(b)}(0) = 0 \tag{3.29}$$

$$\dot{r}_c^{(e)} = v_{eb_c}^{(e)}, \quad r^{(e)}(0) = r_0^{(e)} \tag{3.30}$$

Note that the specific force measurement vector Z enters the mechanization equations linearly. Hence, when the simple Euler integration scheme for the mechanization equations is employed, one can directly use the Δv output of digital accelerometers and solve for the states as:

$$x(k) = x(k-1) + \dot{x}(k) * \Delta t \tag{3.31}$$

where $\dot{x}(k)$ is calculated by inserting the Δv outputs of the accelerometers into the mechanization equations.

3.7 Error Equations Development

We now desire to derive the navigation state error equations for a GF-IMU, which are necessary for the implementation of GF-IMU aiding. The navigation state is denoted by x and the input to the mechanization equations, consisting of the measurements, is denoted by u.

3.7.1 Conventional INS Case. It is first useful to review the development of error equations in a conventional INS before moving on to develop error equations for a GF-INS. In a conventional INS, the navigation state vector x consists of three position variables, three velocity variables, and three attitude angles. The attitude "vector" is denoted by $\mathbf{\Psi} \triangleq [\psi \ \theta \ \phi]^T$ where ψ, θ, and ϕ are the (3,2,1) yaw, pitch, and roll Euler angles, respectively. The measurements of a conventional IMU are the specific force components and the angular rate vector. Thus,

$$x = \begin{pmatrix} r^{(e)} \\ v^{(e)} \\ \Psi \end{pmatrix}_{9 \times 1}, \qquad u = \begin{pmatrix} f^{(b)} \\ \omega_{ib}^{(b)} \end{pmatrix}_{6 \times 1},$$

The kinematics equations relate the navigation state to the specific force and angular rate vectors

$$\dot{x} = f(x, u)$$

The measurement u_m is the sum of the true measurement u and the measurement error δu. The equation is

$$u_m = u + \delta u \tag{3.32}$$

An INS mechanization consists of solving for the calculated navigation states x_c by integrating the kinematics ODE in real-time, which in turn is driven by the input vector u_m. Departing from the kinematics equations, the mechanization equations are written as:

$$\dot{x}_c = f(x_c, u_m), \quad x_c(0) = x_{c_0}, \quad 0 \le t,$$

where the initial navigation state x_{c_0} is determined during the INS initialization/alignment. The error in the navigation state estimate x_c produced by the INS is

$$\delta x \triangleq x_c - x$$

where x is the true navigation state.

To obtain the "error equations", the kinematics function f is expanded to first order

$$f(x, u) = f(x_c, u_m) + \left.\frac{\partial f}{\partial x}\right|_{x_c, u_m} \cdot (x - x_c) + \left.\frac{\partial f}{\partial u}\right|_{x_c, u_m} \cdot (u - u_m) - c \qquad (3.33)$$

$$= f(x_c, u_m) - A \cdot \delta x - \Gamma \cdot \delta u - c \qquad (3.34)$$

where c is the remainder in the Taylor series expansion, and the Jacobians are denoted as:

$$A \triangleq \left.\frac{\partial f}{\partial x}\right|_{x_c, u_m}$$

$$\Gamma \triangleq \left.\frac{\partial f}{\partial u}\right|_{x_c, u_m}$$

Both A and Γ are trajectory-dependent and therefore time-dependent.

We now embark on the development of the error equations.

$$\delta\dot{x} = \dot{x}_c - \dot{x}$$

$$= f(x_c, u_m) - f(x, u)$$

$$= f(x_c, u_m) - f(x_c, u_m) + A \cdot \delta x + \Gamma \delta u + c$$

$$= A\delta x + \Gamma \delta u + c$$

In addition,

$$\delta x(0) = x_c(0) - x(0)$$

3-30

and

$$x_c(0) = x_{c_0}$$

where x_{c_0} is chosen so that

$$x_{c_0} = E(x(0))$$

Indeed, after the INS initialization and alignment, we have

$$x(0) \sim \mathcal{N}(x_{c_0}, P_0) \tag{3.35}$$

and thus

$$\delta x(0) \sim \mathcal{N}(0, P_0) \tag{3.36}$$

Therefore, the navigation state error dynamics are described by the linear stochastic differential equation

$$\delta \dot{x} = \mathbf{A}(t) \cdot \delta x + \mathbf{\Gamma}(t)\delta u + c, \quad \delta x(0) \sim \mathcal{N}(0, P_0)$$

Thus, if we assume the measurement errors are zero-mean and if we neglect the truncation error caused by linearization, c, then the best estimate $\delta \hat{x} \equiv 0$ and therefore the best navigation state estimate is $\hat{x} = x_c$. The use of the mechanization equations is thus justified, since the calculated x_c is the best estimate of the navigation state x. The predicted error in the navigation state estimate x_c provided by the INS has a covariance of $P(t)$ where $P(t)$ is the solution of the Lyapunov equation

$$\dot{\mathbf{P}} = \mathbf{A}\mathbf{P} + \mathbf{P}\mathbf{A}^T + \mathbf{\Gamma}\mathbf{Q}\mathbf{\Gamma}^T, \quad \mathbf{P}(0) = \mathbf{P}_0, \quad 0 \le t \tag{3.37}$$

Q is the intensity of the zero-mean measurement error δu.

3.7.2 GF-INS Case. A GF-INS has an augmented navigation state vector comprising 12 variables and includes the aircraft's angular rate in addition to the standard 9 navigation states of a conventional INS. The input vector u consists

of the N accelerometer measurements and its dimension is equal to the number of accelerometers used. Thus,

$$
x = \begin{pmatrix} r_x \\ r_y \\ r_z \\ v_x \\ v_y \\ v_z \\ \psi \\ \theta \\ \phi \\ \omega_{ib_x} \\ \omega_{ib_y} \\ \omega_{ib_z} \end{pmatrix}, \qquad u = \begin{pmatrix} y_1 \\ \vdots \\ y_N \end{pmatrix}
$$

We will partition the navigation state vector into two separate vectors,

$$
x = \begin{pmatrix} x_1 \\ \dots \\ x_2 \end{pmatrix}
$$

where x_1 consists of the angular and rectilinear velocity state components and x_2 consists of the attitude and position states. Thus,

$$
x_1 = \begin{pmatrix} \omega_{ib}^{(b)} \\ v_{eb}^{(e)} \end{pmatrix}, \qquad x_2 = \begin{pmatrix} \Psi \\ r^{(e)} \end{pmatrix}
$$

By breaking up the state vector we can break up and simplify the process of deriving the state error equations. Recall that the information in the attitude vector Ψ is contained in the $\mathbf{C}_e^b$ DCM. Both x_1 and x_2 have dimension 6. For navigation purposes,

we are interested in $\dot{v}_{eb}$, but we measure and calculate the linear acceleration a. By the Coriolis equation which relates $\dot{v}_{eb}$ to a, Equation (3.4), we now have

$$\dot{v}_{eb}^{(e)} = \mathbf{C}_b^e a^{(b)} + \Omega_E^2 \begin{bmatrix} 1 & 0 & 0 \\ 0 & 1 & 0 \\ 0 & 0 & 0 \end{bmatrix} r^{(e)} - 2\Omega_E \begin{bmatrix} 0 & -1 & 0 \\ 1 & 0 & 0 \\ 0 & 0 & 0 \end{bmatrix} v_{eb}^{(e)} \qquad (3.38)$$

By rearranging the above equation, we have

$$a^{(b)} = \mathbf{C}_e^b \dot{v}_{eb}^{(e)} - \Omega_E^2 \mathbf{C}_e^b \begin{bmatrix} 1 & 0 & 0 \\ 0 & 1 & 0 \\ 0 & 0 & 0 \end{bmatrix} r^{(e)} + 2\Omega_E \mathbf{C}_e^b \begin{bmatrix} 0 & -1 & 0 \\ 1 & 0 & 0 \\ 0 & 0 & 0 \end{bmatrix} v_{eb}^{(e)} \qquad (3.39)$$

Given the output vector u (remember, $u \equiv u_m - \delta u$), the clean variables satisfy

$$u = \mathbf{H} \begin{pmatrix} \dot{\omega}_{ib}^{(b)} \\ a^{(b)} \end{pmatrix} + N(\omega_{ib}^{(b)}) - \mathbf{D} \cdot g^{(b)} \qquad (3.40)$$

Hence, in a GF-IMU the kinematics equations are obtained in descriptor form (a differential equation in which the derivative term on the left side is premultiplied by a term made containing variables) as

$$\mathbf{E}\dot{x}_1 = f_1(x_1, x_2) + u$$
$$\dot{x}_2 = f_2(x_1, x_2)$$

where the full rank matrix

$$\mathbf{E}_{N\times 6} \triangleq \mathbf{H}_{N\times 6} \cdot \begin{bmatrix} I & 0 \\ 0 & \mathbf{C}_e^b(t) \end{bmatrix}_{6\times 6} \qquad (3.41)$$

In order to integrate the kinematics equations, one must first isolate $\dot{x}_1$, and for this one must "invert" the descriptor matrix $\mathbf{E}(t)$.

The GF-IMU geometry optimization criteria can now be validated as regards the matrix $\mathbf{E}$. It is valuable to note that the following proposition holds:

<u>Proposition 1</u>

$$\kappa(\mathbf{E}(t)) = \kappa(\mathbf{H}) = \text{constant for all time}$$

and

$$Tr((\mathbf{E}^T(t)\mathbf{E}(t))^{-1}) = Tr((\mathbf{H}^T\mathbf{H})^{-1})$$

<u>Proof</u>

$$
\begin{aligned}
\mathbf{E}^T(t)\mathbf{E}(t) &=
\begin{bmatrix} \mathbf{I} & 0 \\ 0 & \mathbf{C}_e^{b^T}(t) \end{bmatrix}
\mathbf{H}^T\mathbf{H}
\begin{bmatrix} \mathbf{I} & 0 \\ 0 & \mathbf{C}_e^{b}(t) \end{bmatrix} \\
&=
\begin{bmatrix} \mathbf{I} & 0 \\ 0 & \mathbf{C}_e^{b}(t) \end{bmatrix}^{-1}
(\mathbf{H}^T\mathbf{H})
\begin{bmatrix} \mathbf{I} & 0 \\ 0 & \mathbf{C}_e^{b}(t) \end{bmatrix}
\end{aligned}
$$

Hence, the matrices $\mathbf{E}^T(t)\mathbf{E}(t)$ and $\mathbf{H}^T\mathbf{H}$ are similar. Therefore the spectra of $\mathbf{E}^T(t)\mathbf{E}(t)$ and $\mathbf{H}^T\mathbf{H}$ are identical, which yields $\kappa(\mathbf{E}(t)) = \kappa(\mathbf{H})$. In addition, the inverses of similar matrices are also similar, so that

$$\text{Trace}((\mathbf{E}^T(t)\mathbf{E}(t))^{-1}) = \text{Trace}((\mathbf{H}^T\mathbf{H})^{-1}) \tag{3.42}$$

$\square$

The result is that minimizing $\kappa(\mathbf{H})$ is equivalent to minimizing $\kappa(\mathbf{E}(t))$, and the same applies to the minimization of the GDOP associated with the $\mathbf{H}$ and $\mathbf{E}$ matrices. This validates the choice of the GF-IMU geometry optimization criteria used in Chapter 3.

Returning to the issue of inverting $\mathbf{E}$, since $\mathbf{E}(t)$ is full rank for all time t, the following holds

$$\dot{x}_1 = \mathbf{E}^\dagger \cdot f_1(x_1, x_2) + \mathbf{E}^\dagger u \tag{3.43}$$

$$\dot{x}_2 = f_2(x_1, x_2) \tag{3.44}$$

where the generalized inverse of the descriptor matrix, $\mathbf{E}^\dagger$, is calculated as

$$\mathbf{E}^\dagger = (\mathbf{E}^T \mathbf{E})^{-1} \mathbf{E}^T \tag{3.45}$$

$$= \begin{bmatrix} \mathbf{I} & 0 \\ 0 & \mathbf{C}_e^{b^T}(t) \end{bmatrix} (\mathbf{H}^T \mathbf{H})^{-1} \mathbf{H}^T \tag{3.46}$$

Rewriting the above equations as mechanization equations,

$$\dot{x}_{1_c} = \mathbf{E}^\dagger \cdot f_1(x_{1_c}, x_{2_c}) + \mathbf{E}^\dagger u_m \tag{3.47}$$

$$\dot{x}_{2_c} = f_2(x_{1_c}, x_{2_c}) \tag{3.48}$$

where $u_m \equiv Z$. Thus,

$$\dot{x}_{1_c} = \begin{bmatrix} \mathbf{I} & 0 \\ 0 & \mathbf{C}_e^{b^T}(t) \end{bmatrix} (\mathbf{H}^T \mathbf{H})^{-1} \mathbf{H}^T \cdot f_1(x_{1_c}, x_{2_c}) + \begin{bmatrix} \mathbf{I} & 0 \\ 0 & \mathbf{C}_e^{b^T}(t) \end{bmatrix} (\mathbf{H}^T \mathbf{H})^{-1} \mathbf{H}^T Z \tag{3.49}$$

$$\dot{x}_{2_c} = f_2(x_{1_c}, x_{2_c}), \tag{3.50}$$

that is,

$$\dot{x}_{1_c} = \begin{bmatrix} \mathbf{A}_{\dot\omega} \\ \cdots\cdots \\ \mathbf{C}_{b_c}^e(t)\mathbf{A}_a \end{bmatrix} f_1(x_{1_c}, x_{2_c}) + \begin{bmatrix} \mathbf{A}_{\dot\omega} \\ \cdots\cdots \\ \mathbf{C}_{b_c}^e(t)\mathbf{A}_a \end{bmatrix} Z \tag{3.51}$$

$$\dot{x}_{2_c} = f_2(x_{1_c}, x_{2_c}) \tag{3.52}$$

We note that in the GF-IMU case, the kinematic equations are linear in the forcing signal Z. After linearization, we realize that the state error δx_1 is forced by the measurement noise $\mathbf{E}^{\dagger}\delta u$. Now, the covariance of $\mathbf{E}^{\dagger}\delta u$ is given by

$$
\begin{aligned}
\mathbf{Q} &= E(\mathbf{E}^{\dagger}\delta u \cdot (\mathbf{E}^{\dagger}\delta u)^T) \\
&= E(\mathbf{E}^{\dagger}\delta u \cdot \delta u^T \mathbf{E}^{\dagger^T}) \\
&= \mathbf{E}^{\dagger} \cdot E(\delta u \cdot \delta u^T) \cdot \mathbf{E}^{\dagger^T}
\end{aligned}
$$

We know that
$$
E(\delta u \cdot \delta u^T) = \sigma^2 I_6
$$

Therefore, we calculate

$$
\begin{aligned}
\mathbf{Q} &= \sigma^2 \cdot \mathbf{E}^{\dagger} \cdot \mathbf{E}^{\dagger^T} \\
&= \sigma^2 (\mathbf{E}^T \mathbf{E})^{-1} \cdot \mathbf{E}^T \cdot \mathbf{E} \cdot (\mathbf{E}^T \mathbf{E})^{-1} \\
&= \sigma^2 (\mathbf{E}^T \cdot \mathbf{E})^{-1} \\
&= \sigma^2 \begin{bmatrix} \mathbf{I} & 0 \\ 0 & \mathbf{C}_e^b(t) \end{bmatrix} (\mathbf{H}^T \mathbf{H})^{-1} \begin{bmatrix} \mathbf{I} & 0 \\ 0 & \mathbf{C}_b^e(t) \end{bmatrix}
\end{aligned}
$$

So, by Proposition 1,
$$
Tr(\mathbf{Q}) = Tr(\mathbf{H}^T \mathbf{H})^{-1}.
$$

Hence, minimizing the trace of $(\mathbf{H}^T \mathbf{H})^{-1}$ enhances performance by minimizing the effect of the measurement noise strength $\mathbf{Q}$.

Therefore, similar to the conventional INS case, the mechanization equations have been validated as providing the best estimate of the true navigation state. In addition, this development justifies the optimization of the geometric configuration of the GF-IMU through minimizing $GDOP(\mathbf{H})$ and $\kappa(\mathbf{H})$, since the impact of the measurement error δu on x_1 is minimized.

It is worth briefly comparing the conventional INS mechanization equations with those of the GF-INS. The GF-INS mechanization equations are more complex due to several factors:

1. A GF-INS has 12 navigation states, while a conventional INS has only 9.

2. The kinematics equation of the GF-INS are in descriptor form and the measurement noise is amplified by the regressor matrix $\mathbf{H}$.

3. Unlike a conventional INS for which attitude calculations are independent of gravity, gravitational acceleration enters into the angular rate equation of a GF-INS and consequently error in the gravity field information affects the calculated/estimated attitude.

4. At the same time, the GF-IMU kinematics are linear in the forcing function u, which simplifies the analysis of the stochastic error equations.

3.8 Error Equations for GF-IMU

The navigation state error equations for the GF-IMU equations will now be derived from the GF-IMU mechanization equations, beginning with the attitude error equation. We will start with the error in the DCM, $\delta\mathbf{C}_b^e$, and proceed to derive the error equation that can be used to propagate the attitude error term $\delta\mathbf{\Psi}$

3.8.1 Attitude Error Equation.   The attitude kinematics, as given by Equation (3.25), are

$$\dot{\mathbf{C}}_b^e = \mathbf{C}_b^e \mathbf{\Omega}_{ib}^{(b)} - \mathbf{\Omega}_{ie}^{(e)} \mathbf{C}_b^e$$

Inserting error terms, it can be seen that the error term $\delta\mathbf{\Omega}_{ib}^{(b)}$ causes the error $\delta\mathbf{C}_b^e$ in the $\mathbf{C}_b^e$ DCM. Indeed,

$$\dot{\mathbf{C}}_b^e + \delta\dot{\mathbf{C}}_b^e = (\mathbf{C}_b^e + \delta\mathbf{C}_b^e)(\mathbf{\Omega}_{ib}^{(b)} + \delta\mathbf{\Omega}_{ib}^{(b)}) - \mathbf{\Omega}_{ie}^{(e)}(\mathbf{C}_b^e + \delta\mathbf{C}_b^e) \tag{3.53}$$

Using Equation (3.25) and solving for $\delta\dot{\mathbf{C}}_b^e$, we have

$$\delta\dot{\mathbf{C}}_b^e = \mathbf{C}_b^e \cdot \delta\mathbf{\Omega}_{ib}^{(b)} + \delta\mathbf{C}_b^e \cdot \mathbf{\Omega}_{ib}^{(b)} + \delta\mathbf{C}_b^e \cdot \delta\mathbf{\Omega}_{ib}^{(b)} - \mathbf{\Omega}_{ie}^{(e)} \cdot \delta\mathbf{C}_b^e \qquad (3.54)$$

We now define

$$\delta\mathbf{\Psi} \triangleq -\delta\mathbf{C}_b^e \cdot \mathbf{C}_e^b$$

Note that, to first order (ignoring products of error terms), the matrix $\delta\mathbf{\Psi}$ is skew-symmetric. Therefore, since $\mathbf{C}_b^e$ specifies the aircraft attitude, and $\delta\Psi$ is the attitude error in vector form, one is justified to consider $\delta\mathbf{\Psi}$ the attitude error in skew symmetric form. We can define the error in the DCM as

$$\delta\mathbf{C}_b^e = -\delta\mathbf{\Psi} \cdot \mathbf{C}_b^e \qquad (3.55)$$

Differentiating this equation yields

$$\delta\dot{\mathbf{C}}_b^e = -\delta\dot{\mathbf{\Psi}}\mathbf{C}_b^e - \delta\mathbf{\Psi}\dot{\mathbf{C}}_b^e \qquad (3.56)$$

Inserting Equation (3.25), we have

$$\delta\dot{\mathbf{C}}_b^e = -\delta\dot{\mathbf{\Psi}}\mathbf{C}_b^e - \delta\mathbf{\Psi}\mathbf{C}_b^e\mathbf{\Omega}_{ib}^{(b)} + \delta\mathbf{\Psi}\mathbf{\Omega}_{ie}^{(e)}\mathbf{C}_b^e \qquad (3.57)$$

We now equate Equations (3.54) and (3.57) to obtain

$$-\delta\dot{\mathbf{\Psi}}\mathbf{C}_b^e - \delta\mathbf{\Psi}\mathbf{C}_b^e\mathbf{\Omega}_{ib}^{(b)} + \delta\mathbf{\Psi}\mathbf{\Omega}_{ie}^{(e)}\mathbf{C}_b^e = \mathbf{C}_b^e\delta\mathbf{\Omega}_{ib}^{(b)} + \delta\mathbf{C}_b^e\mathbf{\Omega}_{ib}^{(b)} + \delta\mathbf{C}_b^e\delta\mathbf{\Omega}_{ib}^{(b)} - \mathbf{\Omega}_{ie}^{(e)}\delta\mathbf{C}_b^e \quad (3.58)$$

Solving this for $\delta\dot{\mathbf{\Psi}}$ and applying Lemma 1 we obtain the desired error equation form, which we simplify as follows:

$$\delta\dot{\mathbf{\Psi}} = -\delta\mathbf{\Psi}\mathbf{C}_b^e\mathbf{\Omega}_{ib}^{(b)}\mathbf{C}_e^b + \delta\mathbf{\Psi}\cdot\mathbf{\Omega}_{ie}^{(e)} - \mathbf{C}_b^e\delta\mathbf{\Omega}_{ib}^{(b)}\mathbf{C}_e^b - \delta\mathbf{C}_b^e\mathbf{\Omega}_{ib}^{(b)}\mathbf{C}_e^b - \delta\mathbf{C}_b^e\delta\mathbf{\Omega}_{ib}^{(b)}\mathbf{C}_e^b + \mathbf{\Omega}_{ie}^{(e)}\delta\mathbf{C}_b^e\mathbf{C}_e^b$$

$$= \delta\mathbf{\Psi}(\mathbf{\Omega}_{ie}^{(e)} - \mathbf{C}_b^e\mathbf{\Omega}_{ib}^{(b)}\mathbf{C}_e^b) - \mathbf{C}_b^e\delta\mathbf{\Omega}_{ib}^{(b)}\mathbf{C}_e^b - \delta\mathbf{C}_b^e\mathbf{\Omega}_{ib}^{(b)}\mathbf{C}_e^b - \delta\mathbf{C}_b^e\delta\mathbf{\Omega}_{ib}^{(b)}\mathbf{C}_e^b + \mathbf{\Omega}_{ie}^{(e)}\delta\mathbf{C}_b^e\mathbf{C}_e^b$$

$$= \delta\mathbf{\Psi}(\mathbf{\Omega}_{ie}^{(e)} - \mathbf{\Omega}_{ib}^{(e)}) - \mathbf{C}_b^e\delta\mathbf{\Omega}_{ib}^{(b)}\mathbf{C}_e^b - \delta\mathbf{C}_b^e\mathbf{\Omega}_{ib}^{(b)}\mathbf{C}_e^b - \delta\mathbf{C}_b^e\delta\mathbf{\Omega}_{ib}^{(b)}\mathbf{C}_e^b + \mathbf{\Omega}_{ie}^{(e)}\delta\mathbf{C}_b^e\mathbf{C}_e^b \tag{3.59}$$

Inserting Equation (3.55) into the above equation, again using Lemma 1, we can simplify:

$$\delta\dot{\mathbf{\Psi}} = \delta\mathbf{\Psi}(\mathbf{\Omega}_{ie}^{(e)} - \mathbf{\Omega}_{ib}^{(e)}) - \mathbf{C}_b^e\delta\mathbf{\Omega}_{ib}^{(b)}\mathbf{C}_e^b + \delta\mathbf{\Psi}\mathbf{\Omega}_{ib}^{(e)} - \mathbf{\Omega}_{ie}^{(e)}\delta\mathbf{\Psi} + \delta\mathbf{\Psi}\delta\mathbf{\Omega}_{ib}^{(e)}$$

$$= \delta\mathbf{\Psi}(\mathbf{\Omega}_{ie}^{(e)} - \mathbf{\Omega}_{ib}^{(e)} + \mathbf{\Omega}_{ib}^{(e)}) - \mathbf{C}_b^e\delta\mathbf{\Omega}_{ib}^{(b)}\mathbf{C}_e^b - \mathbf{\Omega}_{ie}^{(e)}\delta\mathbf{\Psi} + \delta\mathbf{\Psi}\delta\mathbf{\Omega}_{ib}^{(e)} \tag{3.60}$$

where $\delta\mathbf{\Psi}\cdot\delta\mathbf{\Omega}_{ib}^{(e)}$ is a higher order term that is ignored. After further simplification of Equation (3.60), we have

$$\delta\dot{\mathbf{\Psi}} = \delta\mathbf{\Psi}\mathbf{\Omega}_{ie}^{(e)} - \mathbf{\Omega}_{ie}^{(e)}\delta\mathbf{\Psi} - \delta\mathbf{\Omega}_{ib}^{(e)} \tag{3.61}$$

Note that, according to Lemma 1, $\mathbf{\Omega}_{ib}^{(e)} = \mathbf{C}_b^e\mathbf{\Omega}_{ib}^{(b)}\mathbf{C}_e^b$ and therefore $\delta\mathbf{\Omega}_{ib}^{(e)} = \mathbf{C}_b^e\delta\mathbf{\Omega}_{ib}^{(b)}\mathbf{C}_e^b$. We now revert back to vector notation, using

$\underline{\text{Lemma 2}}$

$$(\mathbf{A}b)\times = \mathbf{A}\mathbf{B} - \mathbf{B}\mathbf{A}$$

$\square$

We have now derived the attitude error differential equation, which is driven by the error in the angular rate measurements. The final attitude error equation is

$$\delta\dot{\Psi} = -\mathbf{\Omega}_{ie}^{(e)}\delta\Psi - \mathbf{C}_b^e\delta\omega_{ib}^{(b)} \tag{3.62}$$

3.8.2 Angular Rate Error Equation. We now set about deriving the angular rate error equations. We begin by inserting error terms into the mechanization Equation (3.27):

$$\delta\dot{\omega}_{ib}^{(b)} = -\left.\frac{\partial f_{\dot{\omega}}}{\partial \omega_{ib}^{(b)}}\right|_{\omega_{ib_c}^{(b)}}\delta\omega_{ib}^{(b)} + \mathbf{A}_{\dot{\omega}}\mathbf{D}\delta\mathbf{C}_e^b g^{(e)}(r_c^{(e)}) + \mathbf{A}_{\dot{\omega}}\mathbf{D}\,\mathbf{C}_{e_c}^b\left.\frac{\partial g^{(e)}}{\partial r^{(e)}}\right|_{r_c^{(e)}}\delta r^{(e)} + \mathbf{A}_{\dot{\omega}}\delta u \tag{3.63}$$

where

$$\frac{\partial f_{\dot{\omega}}}{\partial \omega} = \mathbf{A}_{\dot{\omega}}\frac{\partial N(\omega_{ib}^{(b)})}{\partial \omega_{ib}^{(b)}} \tag{3.64}$$

We now desire to simplify this equation into a more usable form, so we take the following steps to arrive at the final error equation. Inserting Equation (3.64) into Equation (3.63), we obtain

$$\delta\dot{\omega}_{ib}^{(b)} = \mathbf{A}_{\dot{\omega}}\left[-\frac{\partial N(\omega_{ib}^{(b)})}{\partial \omega_{ib}^{(b)}}\delta\omega_{ib}^{(b)} + \mathbf{D}\delta\mathbf{C}_e^b g^{(e)}(r_c^{(e)}) + \mathbf{D}\mathbf{C}_{e_c}^b\frac{\partial g^{(e)}}{\partial r^{(e)}}\delta r^{(e)} + \delta u\right] \tag{3.65}$$

We know that

$$\delta\mathbf{C}_b^e = -\delta\mathbf{\Psi}\cdot\mathbf{C}_b^e \tag{3.66}$$

We need $\delta\mathbf{C}_e^b$, so we proceed as follows:

$$(\mathbf{C}_b^e + \delta\mathbf{C}_b^e)\cdot(\mathbf{C}_e^b + \delta\mathbf{C}_e^b) = \mathbf{I}$$

$$\Rightarrow$$

$$\mathbf{C}_b^e\cdot\delta\mathbf{C}_e^b \approx -\delta\mathbf{C}_b^e\cdot\mathbf{C}_e^b$$

$$\Rightarrow$$

$$\delta\mathbf{C}_e^b \approx -\mathbf{C}_e^b\delta\mathbf{C}_b^e\mathbf{C}_e^b$$

Using Equation (3.66) yields,

$$\delta \mathbf{C}_e^b \approx -\mathbf{C}_e^b \cdot (-\delta \boldsymbol{\Psi} \cdot \mathbf{C}_b^e) \cdot \mathbf{C}_e^b \tag{3.67}$$

Therefore we have

$$\delta \mathbf{C}_e^b \approx \mathbf{C}_e^b \cdot \delta \boldsymbol{\Psi} \tag{3.68}$$

Inserting Equation (3.68) into Equation (3.65), we obtain the angular rate error equation

$$\delta \dot{\omega}_{ib}^{(b)} = \mathbf{A}_{\dot{\omega}} \left[-\left. \frac{\partial N(\omega_{ib}^{(b)})}{\partial \omega_{ib}^{(b)}} \right|_{\omega_{ib}^{(b)}} \cdot \delta \omega_{ib}^{(b)} + \mathbf{D} \cdot \mathbf{C}_{e_c}^b \cdot \left(\delta \boldsymbol{\Psi} \cdot g^{(e)}(r_c^{(e)}) + \left. \frac{\partial g^{(e)}}{\partial r^{(e)}} \right|_{r_c^{(e)}} \cdot \delta r^{(e)} \right) + \delta u \right] \tag{3.69}$$

Hence, since

$$\delta \boldsymbol{\Psi} \cdot g^{(e)}(r_c^{(e)}) = -g^{(e)}(r_c^{(e)}) \times \delta \boldsymbol{\Psi}$$

$$\boxed{\delta \dot{\omega}_{ib}^{(b)} = \mathbf{A}_{\dot{\omega}} \left[-\left. \frac{\partial N(\omega_{ib}^{(b)})}{\partial \omega_{ib}^{(b)}} \right|_{\omega_{ib}^{(b)}} \delta \omega_{ib}^{(b)} + \mathbf{D}\mathbf{C}_{e_c}^b \left(-g^{(e)}(r_c^{(e)}) \times \delta \boldsymbol{\Psi} + \left. \frac{\partial g^{(e)}}{\partial r^{(e)}} \right|_{r_c^{(e)}} \delta r^{(e)} \right) + \delta u \right]} \tag{3.70}$$

   3.8.3   Velocity and Position Error Equations.   We now turn to the $\dot{v}_{eb}^{(e)}$ equation, Equation (3.29). We will follow the same process as in the two previous sections, in which error terms are inserted into the mechanization equation and then the resulting error equation is simplified into a usable form. Therefore we begin by inserting error terms to this equation as previous done, and then remove the products

of error terms in order to linearize the $\dot{v}_{eb}^{(e)}$ differential equation and obtain

$$\delta\dot{v}_{eb}^{(e)} = \mathbf{C}_{b_c}^{e}\left[-\left.\frac{\partial f_a}{\partial\omega_{ib}^{(b)}}\right|_{\omega_{ib}^{(b)}}\delta\omega_{ib}^{(b)} + \mathbf{A}_a\mathbf{D}\mathbf{C}_{e_c}^{b}\left.\frac{\partial g^{(e)}}{\partial r^{(e)}}\right|_{r_c^{(e)}}\delta r^{(e)} + \mathbf{A}_a\mathbf{D}\delta\mathbf{C}_e^{b}g^{(e)}(r_c^{(e)}) + \mathbf{A}_a\delta u\right]$$

$$+\delta\mathbf{C}_b^{e}\left[-f_a(\omega_{ib_c}^{(b)}) + \mathbf{A}_a\mathbf{D}\mathbf{C}_{e_c}^{b}g^{(e)}(r_c^{(e)}) + \mathbf{A}_au_m\right]-2\Omega_E\begin{bmatrix}0 & -1 & 0\\ 1 & 0 & 0\\ 0 & 0 & 0\end{bmatrix}\delta v_{eb}^{(e)}+\Omega_E^2\begin{bmatrix}1 & 0 & 0\\ 0 & 1 & 0\\ 0 & 0 & 0\end{bmatrix}\delta r^{(e)}$$

$$(3.71)$$

Since

$$f_a = \mathbf{A}_a \cdot N(\omega_{ib}^{(b)}),$$

$$\frac{\partial f_a}{\partial\omega_{ib}^{(b)}} = \mathbf{A}_a \cdot \frac{\partial N(\omega_{ib}^{(b)})}{\partial\omega_{ib}^{(b)}}$$

, substituting these expressions into Equation (3.71) we now have

$$\delta\dot{v}_{eb}^{(e)} = \mathbf{C}_{b_c}^{e}\mathbf{A}_a\left[-\left.\frac{\partial N(\omega_{ib}^{(b)})}{\partial\omega_{ib}^{(b)}}\right|_{\omega_{ib}^{(b)}}\delta\omega_{ib}^{(b)} + \mathbf{D}\mathbf{C}_{e_c}^{b}\left.\frac{\partial g^{(e)}}{\partial r^{(e)}}\right|_{r_c^{(e)}}\delta r^{(e)} + \mathbf{D}\delta\mathbf{C}_e^{b}g^{(e)}(r_c^{(e)}) + \delta u\right]$$

$$+\delta\mathbf{C}_b^{e}\mathbf{A}_a\left[-N(\omega_{ib}^{(b)}) + \mathbf{D}\mathbf{C}_{e_c}^{b}g^{(e)}(r_c^{(e)}) + u_m\right]+2\Omega_E\begin{bmatrix}0 & 1 & 0\\ -1 & 0 & 0\\ 0 & 0 & 0\end{bmatrix}\delta v_{eb}^{(e)}+\Omega_E^2\begin{bmatrix}1 & 0 & 0\\ 0 & 1 & 0\\ 0 & 0 & 0\end{bmatrix}\delta r^{(e)}$$

$$(3.72)$$

We know

$$\delta\mathbf{C}_e^{b} = \mathbf{C}_e^{b} \cdot \delta\mathbf{\Psi},$$

$$\delta\mathbf{C}_b^{e} = -\delta\mathbf{\Psi} \cdot \mathbf{C}_b^{e}$$

These expressions can be inserted into Equation (3.72) to obtain

$$
\delta \dot{v}_{eb}^{(e)} = \mathbf{C}_{b_c}^e \mathbf{A}_a \left[- \left. \frac{\partial N(\omega_{ib}^{(b)})}{\partial \omega_{ib}^{(b)}} \right|_{\omega_{ib}^{(b)}} \delta \omega_{ib}^{(b)} + \mathbf{DC}_{e_c}^b \left. \frac{\partial g^{(e)}}{\partial r^{(e)}} \right|_{r_c^{(e)}} \delta r^{(e)} + \mathbf{DC}_e^b \delta \boldsymbol{\Psi} g^{(e)}(r_c^{(e)}) + \delta u \right]
$$

$$
- \delta \boldsymbol{\Psi} \mathbf{C}_b^e \mathbf{A}_a \cdot \left[-N(\omega_{ib}^{(b)}) + \mathbf{DC}_{e_c}^b g^{(e)}(r_c^{(e)}) + u_m \right] + 2\Omega_E \begin{bmatrix} 0 & 1 & 0 \\ -1 & 0 & 0 \\ 0 & 0 & 0 \end{bmatrix} \delta v_{eb}^{(e)} + \Omega_E^2 \begin{bmatrix} 1 & 0 & 0 \\ 0 & 1 & 0 \\ 0 & 0 & 0 \end{bmatrix} \delta r^{(e)}
$$

$$
\tag{3.73}
$$

This can be rearranged as

$$
\delta \dot{v}_{eb}^{(e)} = \left[\Omega_E^2 \begin{bmatrix} 1 & 0 & 0 \\ 0 & 1 & 0 \\ 0 & 0 & 0 \end{bmatrix} + \mathbf{C}_{b_c}^e \mathbf{A}_a \mathbf{DC}_{e_c}^b \left. \frac{\partial g^{(e)}}{\partial r^{(e)}} \right|_{r_c^{(e)}} \right] \delta r^{(e)} + 2\Omega_E \cdot \begin{bmatrix} 0 & 1 & 0 \\ -1 & 0 & 0 \\ 0 & 0 & 0 \end{bmatrix} \delta v_{eb}^{(e)}
$$

$$
+ \left[(\mathbf{C}_{b_c}^e \mathbf{A}_a \mathbf{DC}_{e_c}^b g^{(e)}(r_c^{(e)})) \times - \mathbf{C}_{b_c}^e \mathbf{A}_a \mathbf{DC}_{e_c}^b (g^{(e)}(r_c^{(e)})) \times + (\mathbf{C}_{b_c}^e \mathbf{A}_a u_m) \times \right] \cdot \delta \boldsymbol{\Psi}
$$

$$
- (\mathbf{C}_{b_c}^e \mathbf{A}_a N(\omega_{ib_c}^{(b)})) \times \cdot \delta \boldsymbol{\Psi} - \mathbf{C}_{b_c}^e \mathbf{A}_a \left. \frac{\partial N}{\partial \omega_{ib_c}^{(b)}} \right|_{\omega_{ib_c}^{(b)}} \delta \omega_{ib}^{(b)} + \mathbf{C}_{b_c}^e \mathbf{A}_a \delta u \quad \tag{3.74}
$$

where the notation $a \times$ denotes the skew symmetric matrix form of the vector a, i.e.,
$a \times = \mathbf{A}$.

Using the matrix Lemma 2,

$$
(\mathbf{C}_{b_c}^e \mathbf{A}_a \mathbf{DC}_{e_c}^b g^{(e)}(r_c^{(e)})) \times = \mathbf{C}_{b_c} \mathbf{A}_a \mathbf{DC}_{e_c}^b (g^{(e)}(r_c^{(e)})) \times - (g^{(e)}(r_c^{(e)})) \times \cdot \mathbf{C}_{b_c}^{(e)} \mathbf{A}_a \mathbf{DC}_{e_c}^b
$$

$$
\tag{3.75}
$$

Inserting Equation (3.75) into Equation (3.74) we obtain

$$\delta \dot{v}_{eb}^{(e)} = \left[\Omega_E^2 \begin{bmatrix} 1 & 0 & 0 \\ 0 & 1 & 0 \\ 0 & 0 & 0 \end{bmatrix} + \mathbf{C}_{b_c}^e \mathbf{A}_a \mathbf{DC}_{e_c}^b \left. \frac{\partial g^{(e)}}{\partial r^{(e)}} \right|_{r_c^{(e)}} \right] \delta r^{(e)}$$

$$+ 2\Omega_E \begin{bmatrix} 0 & 1 & 0 \\ -1 & 0 & 0 \\ 0 & 0 & 0 \end{bmatrix} \delta v_{eb}^{(e)} + \left[-(g^{(e)}(r_c^{(e)})) \times \cdot \mathbf{C}_{b_c}^{(e)} \mathbf{A}_a \mathbf{DC}_{e_c}^b + (\mathbf{C}_{b_c}^e \mathbf{A}_a u_m) \times \right] \delta \Psi$$

$$- (\mathbf{C}_{b_c}^e \cdot \mathbf{A}_a \cdot N(\omega_{ib_c}^{(b)})) \times \cdot \delta \Psi - \mathbf{C}_{b_c}^e \cdot \mathbf{A}_a \cdot \left. \frac{\partial N}{\partial \omega_{ib_c}^{(b)}} \right|_{\omega_{ib_c}^{(b)}} \cdot \delta \omega_{ib}^{(b)} + \mathbf{C}_{b_c}^{(e)} \cdot \mathbf{A}_a \cdot \delta u \quad (3.76)$$

Gravity is calculated using the non-linear κ-filter as

$$g^{(e)} = -\frac{\mu}{r_a^\kappa \cdot r_c^{(3-\kappa)}} \cdot \begin{pmatrix} r_x^{(e)} \\ r_y^{(e)} \\ r_z^{(e)} \end{pmatrix} \quad (3.77)$$

where

$$r_c = \sqrt{r_x^{(e)2} + r_y^{(e)2} + r_z^{(e)2}} \quad (3.78)$$

and r_a is determined from the barometric altitude, if available. If barometric altitude readings are not available, *kappa* is set to 0.

Since we are interested in the error equations, the j_2 term, gravity anomaly, and deflections of the vertical are not considered. The error in the computed gravitational field is caused by the error in the computed position, $\delta r^{(e)}$, and the error in the measured barometric altitude, δh_a. It can be written as

$$\delta g^{(e)} = \frac{\mu \kappa}{r_a^{\kappa+1} r_c^{3-\kappa}} r_c^{(e)} \delta h_a + \frac{\mu \cdot (3-\kappa)}{r_a^\kappa r_c^{5-\kappa}} r_e^{(e)} r_c^{(e)T} \delta r_c^{(e)} - \frac{\mu}{r_a^\kappa r_c^{3-\kappa}} \delta r_c^{(e)}$$

$$= \frac{\mu}{r_a^\kappa r_c^{3-\kappa}} \left[\frac{\kappa}{r_a} r_e^{(e)} \delta h_a + (3-\kappa) \frac{1}{r_c^2} r_c^{(e)} r_c^{(e)T} \delta r_c^{(e)} - \delta r_c^{(e)} \right] \quad (3.79)$$

The following matrix lemma is now used.

<u>Lemma 3</u> Let
$$\mathbf{A} = a \times \text{ and } \mathbf{B} = b\times,$$

then
$$\mathbf{A} \cdot \mathbf{B}{\cdot}c = a^T \cdot c \cdot b - b^T \cdot a \cdot c$$

□

Thus
$$r^{(e)} \cdot r^{(e)T} \cdot \delta r_c^{(e)} = r^{(e)T} \cdot r^{(e)} \cdot \delta r_c^{(e)} + \mathbf{R}^{(e)} \cdot \mathbf{R}^{(e)} \cdot \delta r_c^{(e)}$$

where $\mathbf{R}^{(e)} = r^{(e)} \times$. The error in computed gravity can be written as

$$\delta g^{(e)} = \frac{\mu}{r_a^\kappa \cdot r_c^{3-\kappa}} \cdot \left[\frac{\kappa}{r_a} \cdot r_c^{(e)} \cdot \delta h_a + (2 - \kappa) \cdot \delta r_c^{(e)} + (3 - \kappa) \cdot \frac{1}{r_c^2} \cdot (\mathbf{R}^{(e)})^2 \cdot \delta r_c^{(e)} \right] \quad (3.80)$$

This $\delta g^{(e)}$ term replaces the $\left.\frac{\partial g^{(e)}}{\partial r^{(e)}}\right|_{r_c^{(e)}} \cdot \delta r^{(e)}$ term in the $\delta \dot{v}_{eb}^{(e)}$ equation (and also in the $\delta \dot{\omega}_{ib}^{(b)}$ Equation (3.71), to obtain

$$
\begin{aligned}
\delta \dot{v}_{eb}^{(e)} &= \frac{\mu}{r_a^\kappa r_c^{3-\kappa}} \mathbf{C}_{b_c}^e \mathbf{A}_a \mathbf{D} \mathbf{C}_{e_c}^b \left[(3 - \kappa) \frac{1}{r_c^2} (\mathbf{R}^{(e)})^2 + (2 - \kappa)I \right] \delta r^{(e)} \\
&+ \Omega_E^2 \begin{bmatrix} 1 & 0 & 0 \\ 0 & 1 & 0 \\ 0 & 0 & 0 \end{bmatrix} \delta r^{(e)} + 2\Omega_E \begin{bmatrix} 0 & 1 & 0 \\ -1 & 0 & 0 \\ 0 & 0 & 0 \end{bmatrix} \delta v_{eb}^{(e)} \\
&+ \left[(-g^{(e)}(r_c^{(e)}; r_a, r_c)) \times {\cdot} \mathbf{C}_{b_c}^e \mathbf{A}_a \mathbf{D} \mathbf{C}_{e_c}^b + (\mathbf{C}_{b_c}^{(e)} \mathbf{A}_a u_m) \times \right] \delta \Psi \\
&- (\mathbf{C}_{b_c}^e \mathbf{A}_a \cdot D(\omega_{ib_c}^{(b)})) \times \delta \Psi - \mathbf{C}_{b_c}^e \mathbf{A}_a \left. \frac{\partial N}{\partial \omega_{ib}^{(b)}} \right|_{\omega_{ib_c}} \delta \omega_{ib}^{(b)} + \mathbf{C}_{b_c}^e \mathbf{A}_a \delta u \\
&+ \frac{\mu\kappa}{r_a^{\kappa+1} r_c^{3-\kappa}} \mathbf{C}_{b_c}^{(e)} \mathbf{A}_a \mathbf{D} \mathbf{C}_{e_c}^b r_c^{(e)} \delta h_a \qquad (3.81)
\end{aligned}
$$

Assuming barometric altitude readings are available (which is typically the case in aeronautical applications) and choosing $\kappa = 2$, the final $\delta \dot{v}_{eb}^{(e)}$ error equation is

$$
\delta \dot{v}_{eb}^{(e)} = \frac{\mu}{r_a^2 r_c} \mathbf{C}_{b_c}^e \mathbf{A}_a \mathbf{D} \mathbf{C}_{e_c}^b \left[\frac{1}{r_c^2} (\mathbf{R}^{(e)})^2 + \Omega_E^2 \begin{bmatrix} 1 & 0 & 0 \\ 0 & 1 & 0 \\ 0 & 0 & 0 \end{bmatrix} \right] \cdot \delta r^{(e)}
$$

$$
+ 2\Omega_E \cdot \begin{bmatrix} 0 & 1 & 0 \\ -1 & 0 & 0 \\ 0 & 0 & 0 \end{bmatrix} \delta v_{eb}^{(e)} + \left[-(g^{(e)}(r_c^{(e)}; r_a, r_c)) \times \cdot \mathbf{C}_{b_c}^e \mathbf{A}_a \mathbf{D} \mathbf{C}_{e_c}^b + (\mathbf{C}_{b_c}^{(e)} \mathbf{A}_a u_m) \times \right] \delta \Psi
$$

$$
- (\mathbf{C}_{b_c}^e \mathbf{A}_a N(\omega_{ib_c}^{(b)})) \times \delta \Psi - \mathbf{C}_{b_c}^e \mathbf{A}_a \left. \frac{\partial N}{\partial \omega_{ib}^{(b)}} \right|_{\omega_{ib_c}} \delta \omega_{ib}^{(b)} + \mathbf{C}_{b_c}^e \mathbf{A}_a \delta u
$$

$$
+ \frac{2\mu}{r_a^3 r_c} \mathbf{C}_{b_c}^{(e)} \mathbf{A}_a \mathbf{D} \mathbf{C}_{e_c}^b r_c^{(e)} \delta h_a \tag{3.82}
$$

Note that $\mu = 398600 km^3 sec^{-2}$ is the gravitational constant of Earth and that $\left(\frac{\partial N}{\partial \omega} \right)$ is the following function of ω:

$$
\left(\frac{\partial N}{\partial \omega}(\omega) \right)_i = d_i^T \cdot \begin{bmatrix} \omega_y r_{y_i} + \omega_z r_{z_i} & \omega_x r_{y_i} - 2\omega_y r_{x_i} & \omega_x r_{z_i} - 2\omega_z r_{x_i} \\ \omega_y r_{x_i} - 2\omega_x r_{y_i} & \omega_x r_{x_i} + \omega_z r_{z_i} & \omega_y r_{z_i} - 2\omega_z r_{y_i} \\ \omega_z r_{x_i} - 2\omega_x r_{z_i} & \omega_z r_{y_i} - 2\omega_y r_{z_i} & \omega_x r_{xi} + \omega_y r_{y_i} \end{bmatrix} \tag{3.83}
$$

$i = 1, \dots, N$

Finally, the position error is governed by the simple equation

$$
\delta \dot{r}^{(e)} = \delta v_{eb}^{(e)} \tag{3.84}
$$

The error equations allow one to set up the Lyapunov matrix differential equation, the solution of which yields the predicted covariance of the error in the navigation

states provided by the GF-IMU. One can then predict the performance of the GF-IMU for different accelerometer qualities and array configurations.

3.9   *Chapter Summary*

This chapter began with defining the reading of an individual accelerometer given a specific location and alignment vector in reference to the GF-IMU body frame. From this, we derived the system used to relate the accelerometer measurements to the desired linear and angular accelerations a and $\dot{\omega}$. This system allowed us to determine the conditions for geometric optimality, namely, the condition number of the regressor matrix $\mathbf{H}$ and the Dilution of Precision terms of that same matrix. Next, the mechanization for a GF-IMU was developed using the previously defined system. Finally, the mechanization equations were perturbed with error terms and a set of error equations were developed which could be used in the implementation of GF-IMU aiding.

IV. Results and Analysis

4.1 Overview and Objective

Matlab® was used to simulate the operation of a *stationary* GF-IMU in order to observe the impact of accelerometer grade and GF-IMU geometry on the estimated performance of a GF-IMU. The measurements of the accelerometers making up the GF-IMU are corrupted by random biases, with the goal to observe how far the GF-INS navigation solution wanders from truth for a set amount of time using a certain grade of accelerometers and GF-IMU configuration. The GF-IMU mechanization equations are propagated forward using simulated inputs from accelerometers corrupted by a stable bias. Several GF-IMU accelerometer configurations are tested to allow comparison. The objective of the simulations is to show a proof-of-concept for the theory presented thus far and obtain some "rules of thumb" regarding accelerometer quality, GF-IMU geometry, accelerometer spacing, and performance. The primary questions are:

- Is the accelerometer quality vs. performance relationship linear? For example, do accelerometers with an order of magnitude higher bias values degrade performance by an order of magnitude?

- What insights can be gained by varying the GF-IMU geometry, and do the results support the theory?

- What effect does the GF-IMU array size have on the performance? For example, does doubling the size of the array halve the resultant error magnitude?

In the first set of tests, three separate GF-IMU geometries previously examined in Chapter 3 will be investigated, using five separate grades of accelerometers and a fixed array spacing. In the second set of tests, a single GF-IMU geometry will be investigated using a single grade of accelerometer and a set of five different array sizes.

4.2   Methodology

4.2.1   Simulation Description.   The following assumptions are made:

- The GF-IMU mechanization equations are resolved in the ECEF frame

- A spherical earth is assumed, rotating at $15^o/hour$

- The INS is located at 0 degrees latitude and longitude

- The radius of the earth is given as 6371387 m.

Therefore, the true location of the INS resolved in the ECEF frame is

$$r_0^e = \begin{pmatrix} 0 \\ 0 \\ 6371387 \end{pmatrix} \text{m}$$

The geometry of a GF-IMU is defined as in Chapter 3 by the $\mathbf{D}$ and $\mathbf{R}$ matrices describing the position and sensing directions of the accelerometers relative to the center of the GF-IMU and resolved in the body frame. From this geometry description, the $\mathbf{H}$ and $\mathbf{A}$ matrices can be quickly calculated by computer. The state vector is initialized according to a stationary IMU. The attitude is aligned with the X axis in the ECEF frame, so that the GF-IMU is pointing away from the center of the earth, as in a rocket set to launch perpendicular to the earth's surface. Thus the initial $\mathbf{C}_b^e$ DCM is set to:

$$\mathbf{C}_{b_0}^e = \begin{bmatrix} 1 & 0 & 0 \\ 0 & 1 & 0 \\ 0 & 0 & 1 \end{bmatrix}$$

The inertial angular rate is initialized based on earth rotation. The velocity is initialized at zero. Thus the initial state vector is set to:

$$
x_0 = \begin{pmatrix} \text{Initial Angular Velocity (rad/sec)} \\ \ldots\ldots\ldots \\ \text{Initial Attitude (rad)} \\ \ldots\ldots\ldots \\ \text{Initial Velocity (m/sec)} \\ \ldots\ldots\ldots \\ \text{Initial Position (m)} \end{pmatrix} = \begin{pmatrix} 0 \\ 0 \\ \Omega_E \\ \ldots \\ 0 \\ 0 \\ 0 \\ \ldots \\ 0 \\ 0 \\ 0 \\ \ldots \\ 6378137 \\ 0 \\ 0 \end{pmatrix}
$$

The true states of the stationary IMU do not change. However, due to accelerometer biases, the calculated navigation states based on the measurements will accumulate errors, which are defined by:

$$\text{State Error} = \text{Calculated States} - \text{True States}$$

The forward propagation is accomplished using the simple Euler algorithm, with a time step of 0.01 seconds. That is, each timestep the mechanization equations are used to calculate the $\dot{x}$ vector. More complex forms of propagation yielded insignificant improvements for vastly longer computation times. The updated states are then calculated as:

$$x(\text{new}) = x(\text{old}) + \dot{x} \cdot 0.01 sec$$

Attitude is not directly propagated by the mechanization equations. Instead the Body-to-ECEF DCM is propagated, and the attitude states are backed out each time step using this DCM.

4.2.2 Simulation Parameters.   The flexible set of simulation variables encompasses those values which can be varied to test different scenarios. The list includes:

$10\mu g$	High Quality Navigation Grade
$100\mu g$	Low Quality Navigation Grade
$500\mu g$	Tactical Grade
$1mg$	HG1940 MEMS Grade (future)
$9mg$	HG1900 MEMS Grade (current)

Table 4.1:   Accelerometer Grade Bias Values

1. The number of Monte Carlo runs

2. The length of each Monte Carlo run, in seconds

3. The **R** and **D** matrices describing the geometry used

4. The accelerometer bias variance. Each accelerometer produces measurements corrupted by a randomly generated bias which remains constant during the Monte Carlo run. The bias is generated according to the Gaussian probability function $N(0, \sigma^2)$, where σ^2 represents the accelerometer quality level

5. The size of the GF-IMU, i.e. the distance of the accelerometers or accelerometer triads from the origin

By varying these values it is possible to test the effectiveness of different GF-IMUs geometries using accelerometers of differing qualities.

4.3   Simulation Set 1 Results: Accelerometer Quality Level

A set of 3 geometries are examined, using 5 accelerometer quality levels. The accelerometer quality levels used are given in Table 4.1 and were derived from [23] and [11]. Two levels of navigation-grade accelerometers are used, along with one level of tactical-grade. The HG1900 is a MEMS IMU developed by Honeywell, currently in limited production and use, and has a turn-on bias stability of approximately 9 mg [9]. The HG1940 is a future MEMS IMU currently under development, the approximate specifications of which have been released [9]. In the interest of simplicity, and due to the fact that bias is the dominant error characteristic of accelerometers, no other accelerometer errors are modelled.

4.3.1   Ideal Cube Configuration 1, 'Straight Cube'.

4.3.1.1   Configuration Description.   It is first desired to test a basic cube configuration, utilizing 6 accelerometers, as previously seen in Section 3.4.1. The condition number of the **H** matrix for this configuration was 1, indicating that the accelerometers are ideally positioned to obtain the maximum amount of information about both the angular rotation and the translational acceleration of the body frame. For each Monte Carlo run, a different set of accelerometer biases are generated. 100 total Monte Carlo runs were executed, and the absolute value of the errors averaged (otherwise the error would be zero-mean and the results meaningless). The results are displayed in table form as follows:
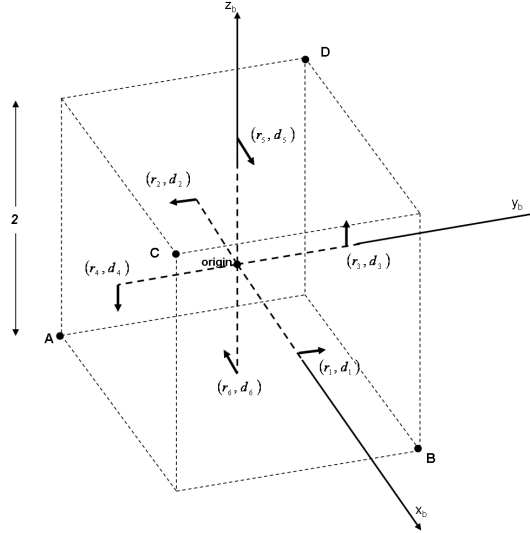

Figure 4.1:   Cube Configuration #1

4.3.1.2   Cube Configuration Simulation Results.

0.01 mg, High Quality Navigation Grade

Length of run (sec)	15	30	45	60
Final angular rate error (deg/sec)	0.0047	0.0108	0.0144	0.0198
Final attitude error (deg)	0.0356	0.1618	0.2269	0.5923
Final position error (m)	0.1572	2.8793	13.37	42.4

0.1 mg, Low Quality Navigation Grade

Length of run (sec)	15	30	45	60
Final angular rate error (deg/sec)	0.0463	0.0989	0.01498	0.1927
Final attitude error (deg)	0.3483	1.4820	3.3541	6.023
Final position error (m)	1.6074	26.78	135.3	408.11

0.5 mg, Tactical Grade

Length of run (sec)	15	30	45	60
Final angular rate error (deg/sec)	0.2444	0.4917	0.8271	DIV
Final attitude error (deg)	1.83	7.41	17.27	DIV
Final position error (m)	7.99	131.5	699.7	DIV

(Simulation diverged after approx. 53 seconds)

1 mg, High Quality MEMS Grade

Length of run (sec)	15	30	45	60
Final angular rate error (deg/sec)	0.4884	1.251	2.1459	DIV
Final attitude error (deg)	3.67	15.5133	33.5	DIV
Final position error (m)	16.9	268.8	1223	DIV

(Simulation diverged after approx. 48 seconds)

9 mg, Low Quality MEMS Grade

Length of run (sec)	15	30	45	60
Final angular rate error (deg/sec)	7.15	DIV	DIV	DIV
Final attitude error (deg)	35.15	DIV	DIV	DIV
Final position error (m)	145.3	DIV	DIV	DIV

4.3.2 Ideal Cube Extension.

4.3.2.1 Configuration Description. The initial cube configuration is now extended by the addition of a triad of accelerometers at the origin. This triad yields additional translational acceleration measurements but no angular rate measurements.
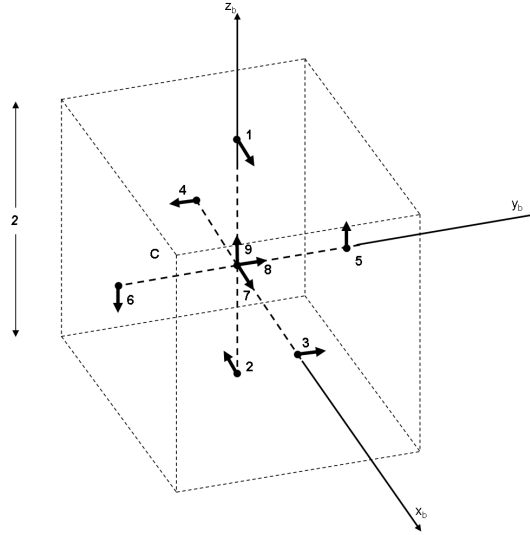

Figure 4.2: 9 Accelerometer Configuration with Triad at Center

4.3.2.2 Cube with Triad at Center Simulation Results.

0.01 mg, High Quality Navigation Grade

Length of run (sec)	15	30	45	60
Final angular rate error (deg/sec)	0.0048	0.0102	.0143	0.0191
Final attitude error (deg)	0.0357	0.1533	0.3221	0.5733
Final position error (m)	0.165	2.7	12.83	42.79

0.1 mg, Low Quality Navigation Grade

Length of run (sec)	15	30	45	60
Final angular rate error (deg/sec)	0.0459	0.0925	0.1375	0.2091
Final attitude error (deg)	0.3443	1.3867	3.0833	6.1867
Final position error (m)	1.595	25.82	131.43	431.2

0.5 mg, Tactical Grade

Length of run (sec)	15	30	45	60
Final angular rate error (deg/sec)	0.2643	0.5142	0.7353	1.2241
Final attitude error (deg)	1.975	7.61	15.58	29.26
Final position error (m)	9.2	139.4	662.0	1964

1 mg, High Quality MEMS Grade

Length of run (sec)	15	30	45	60
Final angular rate error (deg/sec)	0.4911	1.0027	2.2774	DIV
Final attitude error (deg)	3.6593	14.771	33.303	DIV
Final position error (m)	15.94	265.0	1330	DIV

Simulation diverged after approx. 48 seconds

9 mg, Low Quality MEMS Grade

Length of run (sec)	15	30	45	60
Final angular rate error (deg/sec)	8.9842	DIV	DIV	DIV
Final attitude error (deg)	33.92	DIV	DIV	DIV
Final position error (m)	154.6	DIV	DIV	DIV

(Simulation diverged after approx. 18 seconds)

4.3.3   3 Accelerometer Triads.

4.3.3.1   Configuration Description.   This configuration is constructed using three accelerometer triads, arranged on a plane equally distant from a center point and from each other, thus forming an equidistant triangle.
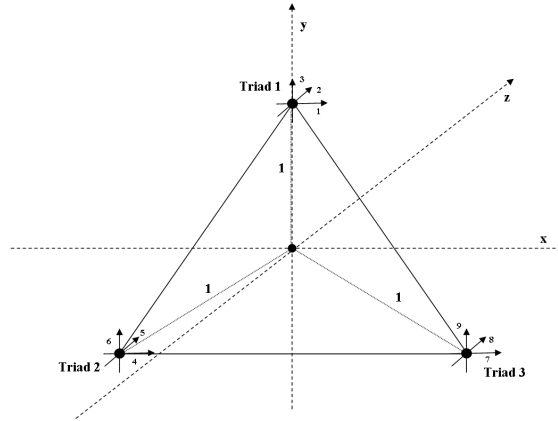

Figure 4.3:   3 Accelerometer Triads

4.3.3.2 Three-Triad Configuration Simulation Results.

0.01 mg, High Quality Navigation Grade

Length of run (sec)	15	30	45	60
Final angular rate error (deg/sec)	0.0046	0.0092	0.0155	0.0205
Final attitude error (deg)	0.0346	0.1382	0.3485	0.6160
Final position error (m)	0.1506	2.400	13.14	41.49

0.1 mg, Low Quality Navigation Grade

Length of run (sec)	15	30	45	60
Final angular rate error (deg/sec)	0.0518	0.1020	0.1591	0.2104
Final attitude error (deg)	0.3888	1.588	3.574	6.2818
Final position error (m)	1.739	26.73	139.8	450.1

0.5 mg, Tactical Grade

Length of run (sec)	15	30	45	60
Final angular rate error (deg/sec)	0.2395	0.5332	0.8057	1.008
Final attitude error (deg)	1.801	8.022	18.36	30.53
Final position error (m)	8.031	140.7	698.9	2060

1 mg, High Quality MEMS Grade

Length of run (sec)	15	30	45	60
Final angular rate error (deg/sec)	0.4911	1.110	1.450	1.767
Final attitude error (deg)	3.665	15.17	32.99	39.97
Final position error (m)	17.06	255.7	1294	3511

9 mg, Low Quality MEMS Grade

Length of run (sec)	15	30	45	60
Final angular rate error (deg/sec)	4.231	8.064	9.887	11.725
Final attitude error (deg)	32.29	35.77	36.78	37.87
Final position error (m)	139.3	1701	4936	10860

Simulation displayed very odd characteristics after about 30 seconds

4.4 Simulation Set 2 Results: GF-IMU Array Size

4.4.1 Test Description.   This set of tests is designed to observe the impact of the geometric size of the GF-IMU array on the performance of the GF-IMU. The assumption is that larger arrays will produce more accurate angular rate measurements due to the larger accelerometer arm-length.

The basic GF-IMU cube geometry is used, and the size is varied based on the size of rigid airframe available in various applications.

1.5 meters	Large aircraft, i.e. bomber or transport
0.5 meter	Small aircraft, i.e. fighter
10 cm	Very small aircraft, i.e. UAV
5 cm	Missile, i.e. air-to-air missile

Table 4.2:   GF-IMU size (approximate radius of array)

1.5 m spacing (large aircraft)

Length of run (sec)	15	30	45	60
Final angular rate error (deg/sec)	0.0321	0.0647	0.1006	0.1341
Final attitude error (deg)	0.2411	0.9693	2.2579	3.975
Final position error (m)	1.10	17.93	91.54	293.9

0.5 meter spacing (small aircraft)

Length of run (sec)	15	30	45	60
Final angular rate error (deg/sec)	0.0997	0.1978	0.3086	0.4013
Final attitude error (deg)	0.748	2.969	6.826	11.68
Final position error (m)	3.415	51.61	272.5	823.6

10 cm spacing (UAV)

Length of run (sec)	15	30	45	60
Final angular rate error (deg/sec)	0.4999	0.9828	DIV	DIV
Final attitude error (deg)	3.724	14.53	DIV	DIV
Final position error (m)	16.69	252.8	DIV	DIV

5 cm spacing (missile)

Length of run (sec)	15	30	45	60
Final angular rate error (deg/sec)	0.9645	3.220	DIV	DIV
Final attitude error (deg)	7.1915	33.49	DIV	DIV
Final position error (m)	33.46	547.06	DIV	DIV

Simulation diverged after approx. 35 seconds

4.5 Analysis

4.5.1 Interpreting the Results. Inertial navigation is extremely trajectory-dependent. It is very important to note that an IMU stationary with respect to the

ECEF frame is in fact moving with respect to the inertial frame. This results in uneven error characteristics, specifically with reference to velocity and position. Positioning the GF-IMU on the X axis resulted in a smaller positional error term along that axis. When the GF-IMU was positioned on the Y axis instead, a similar characteristic was observed with a smaller positional error term along the Y axis. This can be observed in the error growth figures, which demonstrates the characteristic in the position growth plots. The X term in those plots is on average an order of magnitude smaller than the Y or Z terms.

4.5.1.1 Relationship between sensor quality and GF-IMU performance. It can be observed that, with some statistical deviation, the relationship between accelerometer bias and error terms can be approximated as linear under the strict assumptions of this simulation. Accelerometers 10 times worse are likely to diverge 10 times as quickly.

4.5.1.2 Relationship between geometry and performance. In comparing the performance of the cube configuration in Section 4.3.1 with that of the cube extension in Section 4.3.2, it is obvious that the addition of an accelerometer triad at the origin has virtually no effect on performance. Since attitude is the primary limiting factor in a strapdown IMU, and a triad located at the origin contributes nothing toward attitude measurements, this is a reasonable result. Thus the resulting performance is not worth the the added complexity of the additional triad.

The configuration consisting of three accelerometer triads equally spaced from the origin in Section 4.3.3 yielded much more interesting results. In comparison to the cube configuration and utilizing high-grade accelerometers, the triad configuration performed comparably, if slightly worse. However, using lower-grade accelerometers, the triad configuration displayed odd behavior in the angular rate error states, seeming to diverge at a much slower rate after approximately 30 seconds, and at times the error actually appeared to decrease slightly. The resulting position error growth was thus bounded and did not catastrophically diverge as it did in the cube configuration.

The reason for this behavior is not known at this time. It is assumed that, with 9 accelerometers contributing to the angular rate measurements, there would be an "averaging" effect which would reduce the impact of the accelerometer biases over multiple Monte Carlo runs. However, this does not explain the change in the error growth rate of the angular rate state, which remains linear in both other configurations. This result is possibly the result of an unknown numerics or software error. If not, it is possible that a GF-IMU constructed using at least three accelerometer triads, and thus having more than the minimum six accelerometers measuring angular rate, exhibits an a resistance to divergence that is not displayed by either of the cube configurations simulated.

4.5.1.3 The effect of array size. Observing the results of modifying the array size, there appears to be a direct linear relationship between the spacing of the accelerometers from the origin and the GF-IMU performance, within the limited error model examined in these simulations. This is unsurprising as the accelerometer arm-length directly contributes to the magnitude of the angular rate measurement, which allows this measurement to overpower the bias value, increasing the Signal-to-Noise Ratio.

4.5.2 Effect of Gravity Error on a GF-IMU. In a conventional strapdown IMU, the gyroscopes, and thus the propagation of the $\mathbf{C}_b^e$ matrix, are completely independent of the gravity calculations. Thus, even if position information becomes completely useless, the attitude calculations can still be maintained. However, in a GF-IMU, the attitude calculation is dependent on the measurements of accelerometers and thus is dependent on the gravity calculation. Attitude information already degrades an order of magnitude faster due to the additional integration of accelerometer measurement errors. In addition, it degrades further over time due to its dependence on the accuracy of position measurements for the gravity calculation. The net result is that, unlike in a conventional INS, gravity corrupts the attitude states of a GF-IMU over time.

4.5.3 Error Growth Rates.   The introduction of three additional states and an additional integration has the effect of increasing the error growth rate exponentially. This can be observed in Figures 4.4, 4.5, 4.6, and 4.7, which show average error magnitude of each state plotted vs time, as a result of 100 Monte Carlo runs . It can be seen that the angular rate error grows proportional to time t, the attitude error grows proportional to t^2, velocity to t^3, and position to t^4.
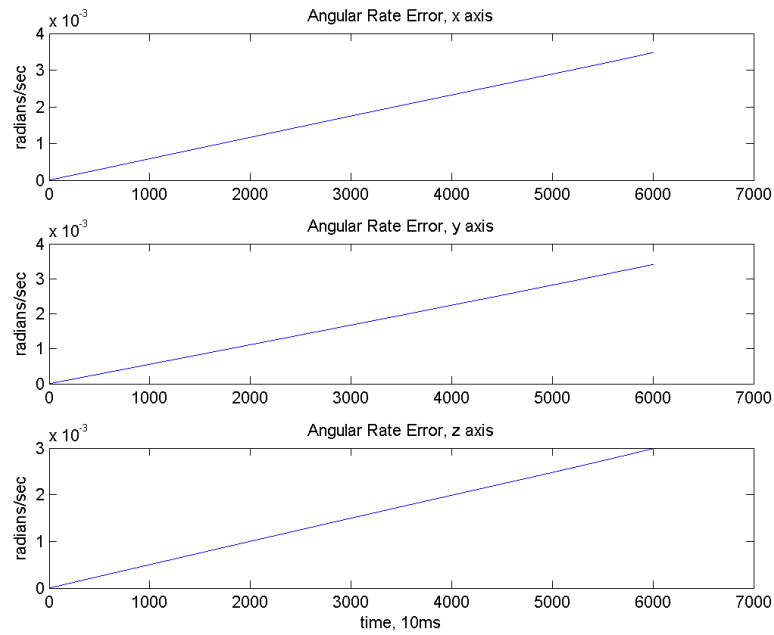
Figure 4.4:   Illustration of Angular Rate Error Growth
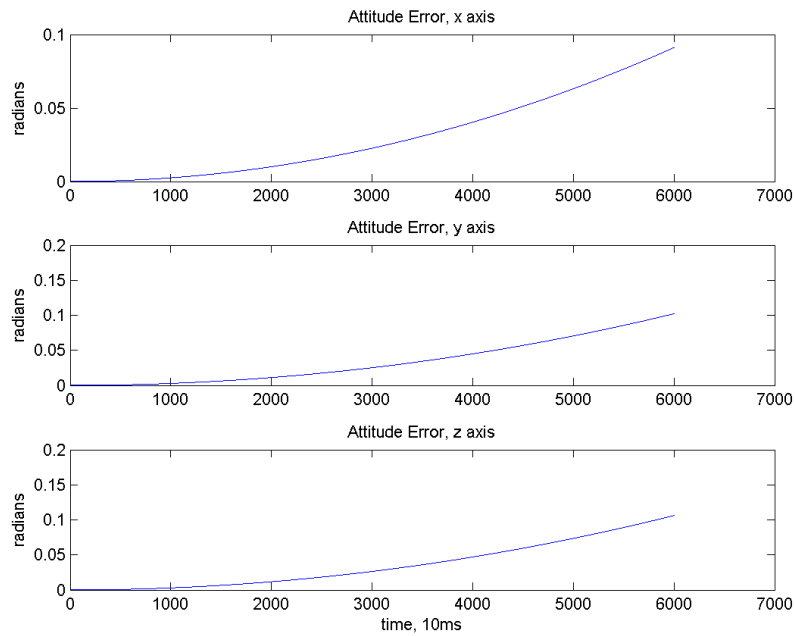

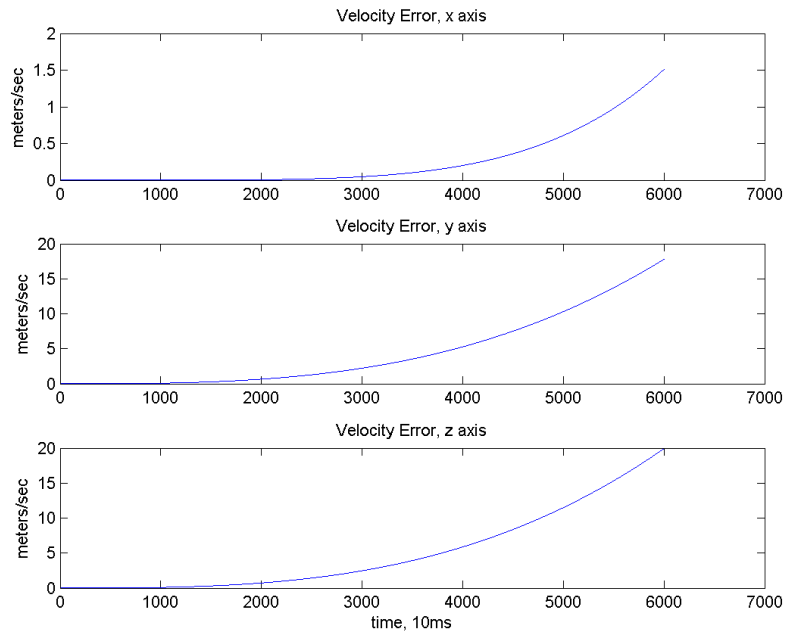Figure 4.5:   Illustration of Attitude Error Growth

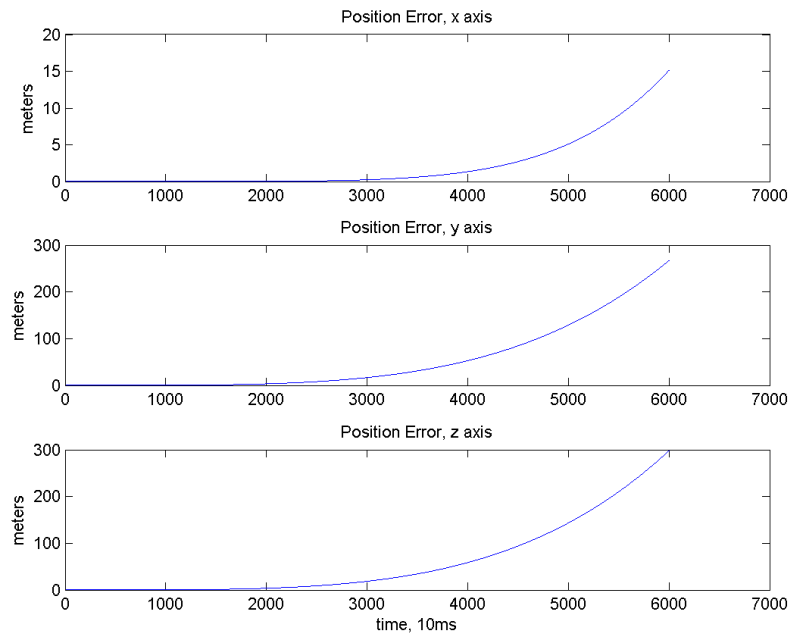Figure 4.6:   Illustration of Velocity Error Growth

Figure 4.7:   Illustration of Position Error Growth

4-17

4.6   Brief Summary

These simulations have functioned as a proof-of-concept for a GF-IMU mechanization. They have demonstrated and validated the estimated error growth characteristics, as well as the qualitative performance estimates based on the condition number of the regressor matrix and the DOP terms defined in Chapter 3. These simulations represent only a minor incursion into the possibilities for simulating a GF-IMU. Future simulations can and should include investigation of the state means and covariances, integration of gyroscope measurements, and introduction of a trajectory.

V. Conclusions

5.1 Summary of Results

This researched has investigated the optimal geometry of a GF-IMU in which an array of accelerometers is used to measure translational and angular acceleration. A linear regression in the acceleration and angular acceleration has been derived. Criteria for scoring different candidate configurations against each other were established: the regressor matrix condition number and the three DOP metrics. Various configurations were developed using the geometry of the Platonic solids and tested using these criteria.

Both six-accelerometer cube configurations, Figures 3.1 and 3.2, yielded $\kappa(\mathbf{H})$ values of 1. A sample third configuration, the tetrahedron configuration in Figure 3.3, yielded a suboptimal result. Hamiltonian path configurations were also considered; some configurations were unusable, and those that were had a suboptimal $\kappa(\mathbf{H})$ of 2. Configurations of nine accelerometers were then considered. The cube configuration was extended by the addition of a triad of accelerometers at the origin; the GDOP was lowered due to the additional measurements, but $\kappa(\mathbf{H})$ became larger because the triad at the origin could not contribute to the angular rate measurements. A non-symmetrical distributed 9 accelerometer configuration produced a suboptimal regressor matrix. Finally, a configuration made up of three accelerometer triads was constructed, applying the principles of optimality thus discovered.

Observing these results, two patterns behind optimality emerge very clearly. The first is the necessity of symmetry in both accelerometer locations and orientations, most easily demonstrated by assuring that the rows of the $\mathbf{R}$ and $\mathbf{D}$ matrices, which describe column by column the position and orientation vectors of each accelerometer, sum to zero. Secondly, the maximum degree of orthogonality is desired between the r and d vectors describing the normalized position and the orientation of each individual accelerometer, thus maximizing the results of the cross product between the two vectors. Normalized r vectors < 1, i.e. those not located on the surface of

a unit sphere, will reduce the magnitude of this cross product and thus result in a larger $\kappa(\mathbf{H})$, thus indicating an inferior geometry.

The optimal geometry for accelerometer positioning can be thus summarized: The accelerometers should be:

1. Equally spaced from the origin of the body frame

2. Positioned for maximum symmetry about all three axes

3. Oriented so that the sensing direction is fully orthogonal to the position vector for each accelerometer.

For configurations of 6, 8, 12, and 20 accelerometers, it can be projected that the optimal locations are defined using the Platonic solids as earlier described.

In the design of a real-life system, these theoretical considerations regarding geometry must be balanced with numerous other considerations pertaining to arm-lengths, ruggedness, reliability, etc. For example, the geometry may be restricted by an oddly shaped airframe, or stretched to allow larger lever-arms in some directions than others so as to make better use of available space/rigidity. The theory developed here provides a sound basis from which to design the geometry of a GF-IMU with a full understanding of its mechanics of operation.

5.2 Application of Results

The application of GF-IMU theory presents a different method of constructing an aided INS. The unaided GF-IMU consists of the 6 or more accelerometers needed to resolve the linear and angular accelerations of the body frame completely, thus providing a set of measurements of the angular acceleration and acceleration. Additional measurements can then be introduced and optimally combined to produce a more accurate navigation system. If full IMUs are used to construct the GF-IMU, the gyroscope measurements about each axis can be averaged and then treated as direct measurements of the angular rate states.
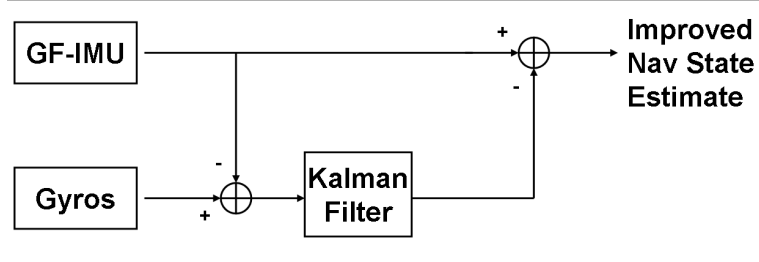
Figure 5.1:   Diagram of Gyroscope Aiding

The resultant system therefore derives its angular rotation from a combination of the angular acceleration measurements provided by the GF-IMU and the average of the rate gyro measurements. The angular rate measurements are thus somewhat improved from the individual IMU measurements. Although this development has been accomplished with MEMS in mind, it is in no way limited to use with low-quality IMUs. Any system which utilizes multiple IMUs can benefit from the application of this theory.

5.3   Future Work

This research has only scraped the surface of simulating and estimating the performance of a GF-IMU. Using the groundwork laid in this thesis, the next logical step is the development of a more complex and realistic navigation filter implementation, allowing for the optimal combination of gyroscope measurements with the GF-IMU states. This can be accomplished using a simple Kappa-type or Alpha -type filter or a more complex Kalman filter capable of also combining GPS measurements and accounting for error characteristics. Using this filter and a more refined error model as well as a variety of aircraft trajectories, it would be possible to gain a more accurate understanding of the potential performance gained. If the results are promising, it would then be possible to then construct a prototype to run real-life tests.

Bibliography

1. "A – Antenna Advanced Inertial Reference for Enhanced Sensors (ANTARES)". *FBO Daily*, FBO 0499 (April 13 2003):465–471, 8 March 2005. URL `http://www.fbodaily.com/archive/2003/04-April/13-Apr-2003/FBO-00301795.htm`.

2. Bourne, M. "Gyros to go: Sensors Will Keep Moving for Military, Auto". *Small Times*, February 20 2004.

3. Brown, A.K. *"Test Results of a GPS/Inertial Navigation System Using a Low Cost MEMS IMU"*. Technical report, NAVSYS Corporation, 14960 Woodcarver Road, Colorado Springs CO 80921 USA, April 2001.

4. Chen, Jeng-Heng, Sou-Chen Lee, and Daniel B. DeBra. "Gyroscope Free Strapdown Inertial Measurement Unit by Six Linear Accelerometers". *Journal of Guidance, Control, and Dynamics*, Vol. 17, No. 2:286–290, March-April 1994.

5. Cowley, G. "The Biology of Beauty". *Newsweek*, Vol. 127, No. 23:60–67, June 3, 1996.

6. *EX 171 Extended Range Guided Munition*. Technical report, Raytheon Company, 2004.

7. *Fact Sheet: Organic Air Vehicle Program (July 2001)*. Technical report, Defense Advanced Research Projects Agency, 8 March 2005. URL `http://www.darpa.mil/body/NewsItems/pdf/OAVcontractorsfs.pdf`.

8. Faisal, Mohd-Yasin, Can E. Korman, and David J. Nagel. *Measurement of Noise Characteristics of MEMS Accelerometers*. Technical report, Department of Electrical and Computer Engineering, The George Washington University, Washington DC 20052 District of Colubmia, 2002.

9. Hanse, J.G. "Honeywell MEMS Inertial Technology and Product Status". April 2004.

10. LeFevre, V. and D. Panhorst. "Common Guidance Common Sense". *NDIA Firepower Symposium (June 2004)*, 8 March 2005. URL `www.dtic.mil/ndia/2004armaments/DayII/SessionI/05_Panhorst_MEMS_in_Weapons.pdf`.

11. Levy and Pue. "Integration of GPS with Inertial Navigtion Systems". September 2001.

12. Maybeck, Peter S. *Stochastic Models, Estimation, and Control Volume 2*. Academic Press, Inc., New York NY, 1982.

13. Maybeck, Peter S. *Stochastic Models, Estimation, and Control Volume 3*. Academic Press, Inc., New York NY, 1982.

14. Maybeck, Peter S. *Stochastic Models, Estimation, and Control Volume 1*. Navtech Book and Software Store, Arlington VA, 1994.

15. McKay, J.B. and M. Pachter. "Geometry Optimization for GPS Navigation". December 1997.

16. Mehregany, M. and S. Roy. *Microengineering Aerospace Systems*. Technical report, The Aerospace Corporation, 1999.

17. Neubert, K. "Platonic Spheres". 8 March 2005. URL `http://www.neubert.net/PLASpher.html`.

18. Pachter, M. and J.B. McKay. "Geometry Optimization of a GPS-based Navigation Reference System". *Journal of the Institute of Navigation*, Vol. 44, No. 4:457–490, Winter 1997-1998.

19. Padgaonkar, A.J., K.W. Krieger, and A.I. King. "Measurement of Angular Acceleration of a Rigid Body Using Linear Accelerometers". *Journal of Applied Mechanics, Transaction of the American Society of Mechanical Engineers*, Vol. 42:552–556, September 1975.

20. Park, Sungsu and Chin-Woo Tan. *GPS-Aided Gyroscope-Free Inertial Navigation Systems*. Contract UCB-ITS-PRR-2002-22, California PATH Program, Institute of Transportation Studies, University of California, Berkeley, UC Berkeley CA, June 2002.

21. Rogers, R.M. *Applied Mathematics in Integrated Navigation Systems*. American Institute of Aeronautics and Astronautics, Inc., Reston VA, 2000.

22. Schuler, A.R., A. Grammatikos, and K.A. Fegley. "Measuring Rotational Motion with Linear Accelerometers". *IEEE Transactions on Aerospace and Electronic Systems*, Vol. AES-3, No. 3:465–471, 1967.

23. Schwarz and El-Sheimy. *Future Positioning and Navigation Technologies, POS/NAV Project*. Technical report, Department of Geomatics Engineering, University of Calgary, 1999.

24. "Star Tracker Stellar Compass (STSC)". UCRL-TB-119860 (September 1995), 8 March 2005. URL `http://www.llnl.gov/sensor_technology/STR45.html`.

25. Tan, C., S. Park, K. Mostov, and P. Varaiya. "Design of Gyroscope-Free Navigation Systems". August 2001.

26. Tan, Chin-Woo and Sungsu Park. *"Design and Error Analysis of Accerometer-Based Inertial Navigation Systems"*. Contract UCB-ITS-PRR-2002-21, California PATH Program, Institute of Transportation Studies, University of California, Berkeley, UC Berkeley CA, June 2002.

27. Titterton, D.H. and J.L. Weston. *Strapdown Inertial Navigation Technology*. Academic Press, Inc., Herts. United Kingdom, 1997.

28. Wu, William. *The Platonic Solids*. Technical report, UC Berkeley, 8 March 2005. URL `http://www.ocf.berkeley.edu/~wwu/papers/platonicsolids.pdf`.

29. *XM982 Precision-Guided, Long Range, 155mm Artillery Projectile.* Technical report, Raytheon Company, 2003.

30. Zelek, J. *Bayesian Real-time Optical Flow.* Technical report, School of Engineering, University of Guelph, Guelph ON, N1G 2W1, Canada, 2002.

REPORT DOCUMENTATION PAGE			*Form Approved* *OMB No. 074-0188*

The public reporting burden for this collection of information is estimated to average 1 hour per response, including the time for reviewing instructions, searching existing data sources, gathering and maintaining the data needed, and completing and reviewing the collection of information. Send comments regarding this burden estimate or any other aspect of the collection of information, including suggestions for reducing this burden to Department of Defense, Washington Headquarters Services, Directorate for Information Operations and Reports (0704-0188), 1215 Jefferson Davis Highway, Suite 1204, Arlington, VA 22202-4302. Respondents should be aware that notwithstanding any other provision of law, no person shall be subject to an penalty for failing to comply with a collection of information if it does not display a currently valid OMB control number.
PLEASE DO NOT RETURN YOUR FORM TO THE ABOVE ADDRESS.

1. REPORT DATE *(DD-MM-YYYY)* 21-03-2005	**2. REPORT TYPE** **Master's Thesis**	**3. DATES COVERED** *(From – To)* Sept 2003- Mar 2005

4. TITLE AND SUBTITLE Using Multiple MEMS IMUs to form a Distributed Inertial Measurement Unit	**5a. CONTRACT NUMBER**
	5b. GRANT NUMBER
	5c. PROGRAM ELEMENT NUMBER
6. AUTHOR(S) Hanson, Ryan D., 2nd Lieutenant, USAF	**5d. PROJECT NUMBER**
	5e. TASK NUMBER
	5f. WORK UNIT NUMBER

7. PERFORMING ORGANIZATION NAMES(S) AND ADDRESS(S) Air Force Institute of Technology Graduate School of Engineering and Management (AFIT/EN) 2950 Hobson Way WPAFB OH 45433-7765	**8. PERFORMING ORGANIZATION REPORT NUMBER** AFIT/GE/ENG/05-06

9. SPONSORING/MONITORING AGENCY NAME(S) AND ADDRESS(ES) Dr. Mikel Miller AFRL/SNRP 2241 Avionics Circle WPAFB OH 45433-7318 786-6127 x4274	**10. SPONSOR/MONITOR'S ACRONYM(S)**
	11. SPONSOR/MONITOR'S REPORT NUMBER(S)

12. DISTRIBUTION/AVAILABILITY STATEMENT
 APPROVED FOR PUBLIC RELEASE; DISTRIBUTION UNLIMITED.

13. SUPPLEMENTARY NOTES

14. ABSTRACT
 MEMS IMUs are readily available in quantity and have extraordinary advantages over conventional IMUs in size, weight, cost, and power consumption. However, the poor performance of MEMS IMUs limits their use in more demanding military applications. It is desired to use multiple distributed MEMS IMUs to simulate the performance of a single, more costly IMU, using the theory behind Gyro-Free IMUs. A Gyro-Free IMU (GF-IMU) uses a configuration of accelerometers only to measure the three accelerations and three angular rotations of a rigid body in 3-D space. Theoretically, almost any configuration of six distributed accelerometers yields sufficient measurements to solve for the translational and angular acceleration. In reality, however, sensor noise corrupts the measurements and good sensor geometry is necessary to obtain an accurate estimate of the translational and angular accelerations. Determining the optimal configuration of accelerometers is an exercise in geometry. This thesis investigates the optimal geometry of an INS constructed of multiple networked IMUs and develops the accompanying mechanization and error equations. Simple simulations are run to test and validate the basic design principles.

15. SUBJECT TERMS
Inertial Navigation, Inertial Measurement Units, Optimization, Navigation

16. SECURITY CLASSIFICATION OF:			**17. LIMITATION OF ABSTRACT**	**18. NUMBER OF PAGES**	**19a. NAME OF RESPONSIBLE PERSON** Dr. Meir Pachter, AFIT/ENG
REPORT **U**	**ABSTRACT** **U**	**c. THIS PAGE** **U**	**UU**	105	**19b. TELEPHONE NUMBER** *(Include area code)* (937) 785-6565 x4280

Standard Form 298 (Rev: 8-98)
Prescribed by ANSI Std. Z39-18